



Review

Powerful combination of MOFs and C_3N_4 for enhanced photocatalytic performance

Chong-Chen Wang*, Xiao-Hong Yi, Peng Wang

Beijing Key Laboratory of Functional Materials for Building Structure and Environment Remediation/Beijing Advanced Innovation Center for Future Urban Design, Beijing University of Civil Engineering and Architecture, Beijing, 100044, China

ARTICLE INFO

Keywords:

Metal-organic frameworks
Carbon nitride
Photocatalysis
Heterojunction
Visible light

ABSTRACT

Both pristine metal-organic frameworks (MOFs) and graphitic carbon nitride ($g-C_3N_4$) displayed outstanding photocatalytic performances toward H_2 production, CO_2 reduction, Cr(VI) reduction and organic pollutants degradation. To further enhance their photocatalytic performances under visible light or sunlight irradiation, MOFs and $g-C_3N_4$ were combined to construct $g-C_3N_4$ /MOF heterojunctions with the purpose of overcoming their individual disadvantages like fast recombination of photogenerated electron-hole pairs. The fabrication methods, characterizations, photocatalytic performances and the corresponding mechanism of some typical $g-C_3N_4$ /MOF composites were highlighted. Also, the prospective and challenges of this research field were declared.

1. Introduction

Metal-organic frameworks (MOFs), as highly porous crystalline materials constructed from metal templates and organic linkers, have attracted increasing attentions due to their potential applications of catalysis [1–3], energy gas storage [4–6], gas separation [7–9], adsorption toward pollutants [10–18], and so on [19–27]. Especially, a range of MOFs with good photocatalytic activities have been investigated by increasing researchers with great enthusiasm [28–42], since the first work made by García and coworkers on the photocatalytic phenol photodegradation by adopting MOF-5 as a semiconductor under UV light irradiation in 2008 [43]. Over the past decade, the potential photocatalysis application of MOFs arose growing attentions due to the synergistic effect of their metal centers and organic linkages [29]. As to the photocatalytic activities of MOFs, some papers provided comprehensive and critical review on their applications to conduct water splitting, CO_2 reduction, Cr(VI) reduction and organic pollutants degradation [28,29,31,41,42,44–52]. However, most MOFs exhibited efficiently photocatalytic performances only under the UV light illumination, which limited their wide potential applications under visible light or sunlight. Also, some problems like the poor conductivity, inadequate stabilities and fast electron-hole recombination limited the MOF's potential use as photocatalysts [28]. Generally, three strategies like the introduction of $-NH_2$ group, synthesis of Fe-containing MOFs and the construction of heterostructures with the aid of

narrow gap semiconductors were adopted to modify MOFs utilize the visible light or even sunlight [28,29,39,53–59]. However, some ligands are difficult to introduce $-NH_2$ group at ideal sites, or the introduced $-NH_2$ group would change the ligands' original coordination mode. Therefore, it is not always feasible to modify functional groups on organic ligands. As well, most Fe-containing MOFs displayed good photocatalytic performance under visible light irradiation due to the extensive Fe-O (iron-oxo) clusters [58,59]. However, the diversity of MOFs required more metal ions besides Fe to be selected as templates. The third strategy to construct heterostructures between narrow gap semiconductors and MOFs was more preferred to excite their photocatalytic activity under visible light or sunlight [28,29,60].

Another star photocatalyst is polymeric graphite-like C_3N_4 ($g-C_3N_4$), a metal-free semiconductor, which is an outstanding photocatalyst due to: (1) π -conjugated electronic structures [61,62]; (2) the band gap of ca. 2.7 eV (conduction band, ca. -1.1 V vs. NHE; valence band, ca. 1.6 V vs. NHE), implying it can absorb visible light [63,64]; (3) its outstanding chemical stability in solutions of any pH under light illumination along with its excellent thermal stability [65,66]; (4) its low cost due to that it can be produced from relatively cheap N containing organic precursors like urea, melamine and so on [67–71]; and (5) convenient and facile synthesis routes [72–80]. Therefore, $g-C_3N_4$ has been widely applied in diverse fields like catalysis [67,81,82], water splitting [83–86], CO_2 reduction [83,87,88], Cr(VI) reduction [89–93], and photocatalytic degradation of organic pollutants [94–96]. However, the

* Corresponding author.

E-mail address: wangchongchen@bucea.edu.cn (C.-C. Wang).<https://doi.org/10.1016/j.apcatb.2019.01.091>

Received 16 November 2018; Received in revised form 9 January 2019; Accepted 31 January 2019

Available online 02 February 2019

0926-3373/© 2019 Elsevier B.V. All rights reserved.

Table 1The photocatalytic performances of some binary MOF/g-C₃N₄ composites.

Composites	Preparation method	Applications	Ref.
g-C ₃ N ₄ /ZIF-8	In-situ deposition of ZIF-8 from its precursors on the prepared g-C ₃ N ₄ nanotubes	CO ₂ reduction	[109]
g-C ₃ N ₄ /ZIF-8	In-situ deposition of ZIF-8 nanoparticles from its precursors on the prepared g-C ₃ N ₄ .	H ₂ production	[110]
g-C ₃ N ₄ /ZIF-8	In-situ deposition of ZIF-8 from its precursors on the prepared g-C ₃ N ₄ .	Adsorption and photocatalytic degradation toward tetracycline	[111]
ZIF-8/g-C ₃ N ₄	In-situ deposition of ZIF-8 from its precursors on the prepared g-C ₃ N ₄ .	Rhodamine B (RhB) degradation	[112]
g-C ₃ N ₄ /UiO-66	Annealing the mixture of prepared UiO-66 octahedrons and g-C ₃ N ₄	H ₂ production	[107]
g-C ₃ N ₄ /UiO-66	(i) The carbon nitride nanosheets (CNNS) were prepared by a liquid exfoliation route from bulk carbon nitride (CN) in water. (ii) The CNNS were coated on as-prepared UiO-66 via electrostatic interactions.	CO ₂ reduction	[108]
g-C ₃ N ₄ /UiO-66	Solvothermal deposition of UiO-66 on the prepared g-C ₃ N ₄	RhB degradation	[113]
g-C ₃ N ₄ /UiO-66	thermal treating the mixture of UiO-66 octahedrons and g-C ₃ N ₄ sheets	Methylene blue (MB) degradation	[114]
g-C ₃ N ₄ /MIL-53(Al)	Solvothermal deposition of MIL-53(Al) on the prepared g-C ₃ N ₄	RhB degradation	[115]
g-C ₃ N ₄ /MIL-53(Fe)	Solvothermal deposition of MIL-53(Fe) on the prepared g-C ₃ N ₄	Cr(VI) reduction	[9]
g-C ₃ N ₄ /MIL-53(Fe)	Grinding between prepared MIL-53(Fe) and g-C ₃ N ₄	H ₂ production	[116]
g-C ₃ N ₄ /MIL-100(Fe)	In-situ chemical protonation of g-C ₃ N ₄ and dip-coating between the prepared MIL-100(Fe) and g-C ₃ N ₄ mixture via thermal treatment.	RhB and MB degradation, along with the oxidative denitrogenation towards pyridine	[117]
C ₃ N ₄ /MIL-100(Fe)	In-situ deposition of MIL-100(Fe) nanoparticles from its precursors on the prepared carbon nitride nano-sheet (CNNS).	RhB degradation	[118]
MIL-100(Fe)/g-C ₃ N ₄	Ball-milling and thermal treatment of prepared g-C ₃ N ₄ and MIL-100(Fe) mixture.	Cr(VI) reduction	[119]
g-C ₃ N ₄ /NH ₂ -MIL-101(Fe)	In-situ deposition of MIL-101(Fe) from its precursors on the prepared g-C ₃ N ₄	Cr(VI) reduction and methyl orange (MO) degradation	[120]
g-C ₃ N ₄ /MIL-101(Fe)	In-situ hydrothermal synthesis of MIL-101(Fe), which can be covered by the prepared g-C ₃ N ₄ .	Bisphenol A (BPA) degradation.	[121]
g-C ₃ N ₄ /MIL-125(Ti)	In-situ deposition of MIL-125(Ti) from its precursors on the prepared g-C ₃ N ₄	RhB degradation	[122]
g-C ₃ N ₄ /CuBTC	In-situ deposition of CuBTC from its precursors on the prepared g-C ₃ N ₄	Dimethyl chlorophosphate (DMCP) degradation	[123]
g-C ₃ N ₄ /NH ₂ -MIL-88B(Fe)	In-situ deposition of NH ₂ -MIL-88B(Fe) from its precursors on the prepared g-C ₃ N ₄ .	MB degradation	[124]
g-C ₃ N ₄ /MIL-88B(Fe)	In-situ fabrication of MIL-88B(Fe) from its precursor on the prepared g-C ₃ N ₄ nanosheets.	MB degradation and Cr(VI) reduction.	[125]
g-C ₃ N ₄ /BUC-21	Ball-milling of prepared g-C ₃ N ₄ and BUC-21.	Cr(VI) reduction	[126]

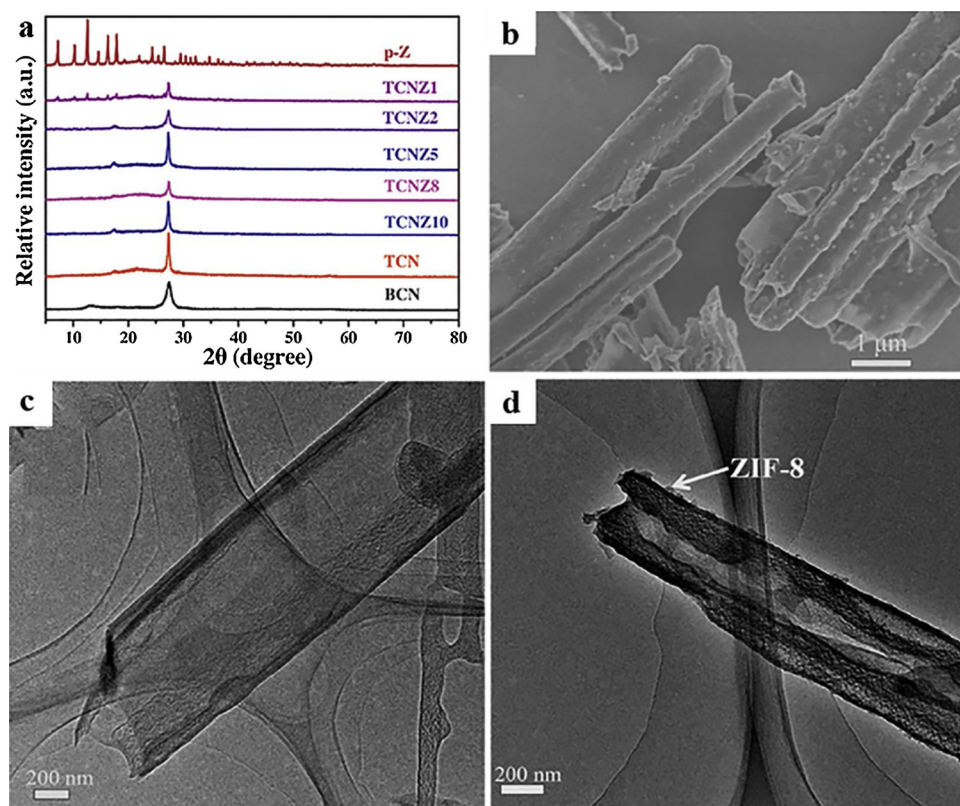


Fig. 1. (a) PXRD patterns of the as-prepared bulk g-C₃N₄ (BCN), tubular g-C₃N₄ (TCN), ZIF-8 nanocluster (p-Z), and series g-C₃N₄/ZIF-8 composites (TCNZx, x is the initial mass ratio of g-C₃N₄ to ZIF-8); (b) The FESEM image of TCN; (c) and (d) The TEM images of TCN and g-C₃N₄/ZIF-8 (TCNZ8, the initial mass ratio is 8) [109], copyright (2017) Elsevier.

further practical application of pristine g-C₃N₄ also suffered from its intrinsic drawbacks: (i) its easy recombination of photogenerated electron-hole pairs due to the hybridization of the N 2p and C 2p states in the CB and unavoidably disordered structure or defects [6,97,98]; (ii) limited visible light utilization due to its moderate bandgap

($E_g = 2.7$ eV, corresponding to an optical wavelength of 460 nm); (iii) its low surface area resulted from its bulk structure [99–101], and (iv) poor hydrophilicity. Some strategies were adopted to improve the photocatalytic performance of g-C₃N₄, which could be classified into electronic structure modification [102,103], nanostructure design [104],

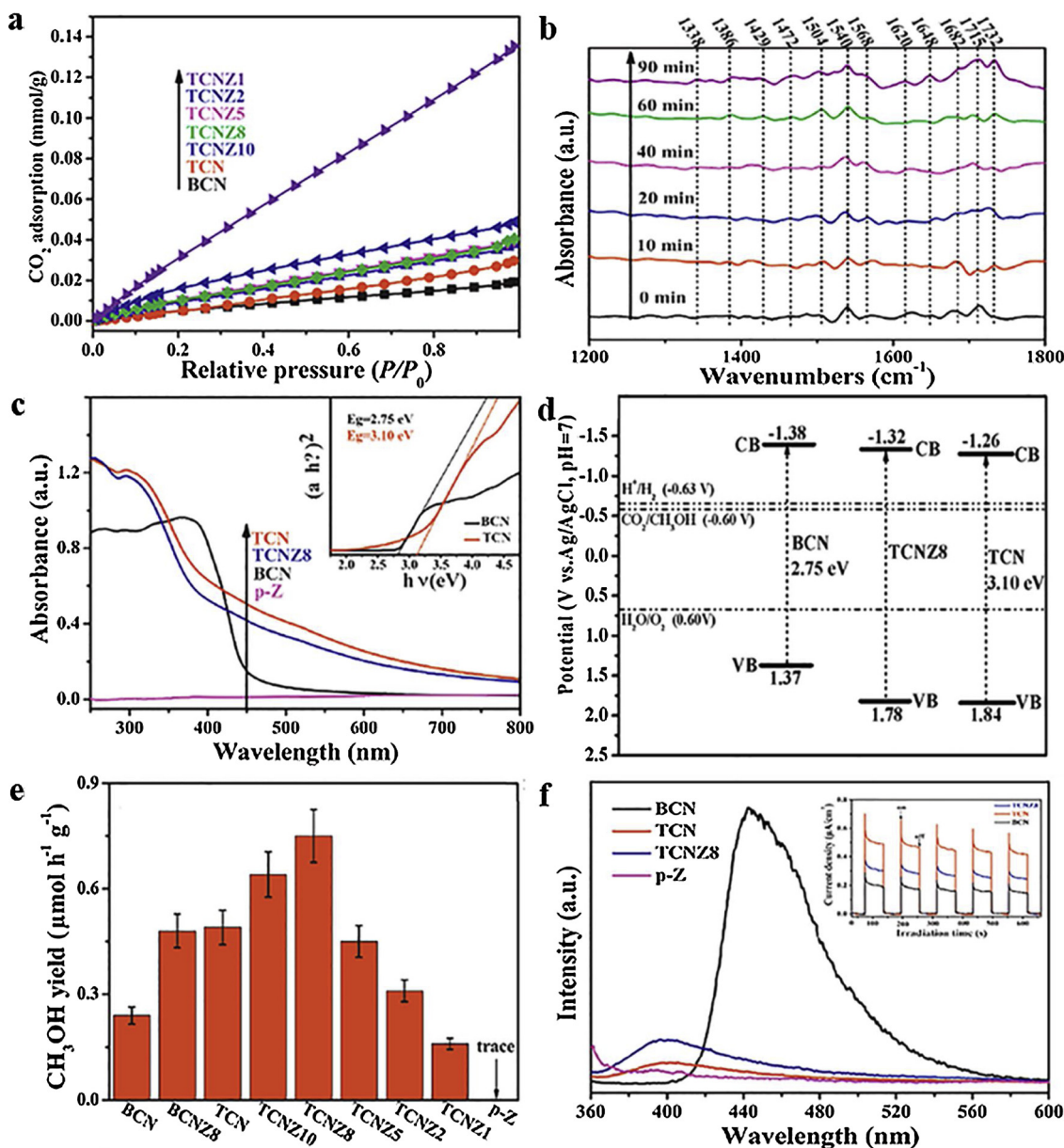


Fig. 2. (a) CO₂ adsorption curves of bulk g-C₃N₄ (BCN), nanotubular g-C₃N₄ (TCN), and series g-C₃N₄/ZIF-8 (TCNZ_x) composites; (b) The in situ FTIR spectra of g-C₃N₄/ZIF-8 (TCNZ8, the initial mass ratio is 8) in a flow of CO₂/H₂O vapor matrix as a function of irradiation time; (c) UV-vis DRS of the BCN, TCN, ZIF-8 nanocluster and TCNZ8 and the estimated band gap energies of BCN and TCN (inset); (d) Band alignments for typical samples. The bandgap was estimated from UV-vis diffuse reflectance spectra, and CB was estimated from the Mott-Schottky plots; (e) The CH₃OH generation rate of different as-prepared samples; (f) The PL spectra of as-prepared samples and transient photocurrent responses for the BCN, TCN, and TCNZ8 samples (inset) [109], copyright (2017) Elsevier.

crystal structure engineering [105] and heterostructure construction [106].

It is generally deemed that a desired photocatalyst should simultaneously possess the merits of suitable bandgap, proper hydrophilicity, large surface area and cost-effective. To overcome the drawbacks of MOFs and g-C₃N₄, and to achieve the merits of ideal photocatalysts for enhanced photocatalytic performances, the fabrication of binary g-C₃N₄/MOF and ternary g-C₃N₄/MOF/X (X is one of semiconductor photocatalysts) heterojunction composites in both macroscale and nanoscale has been proved as an effective strategy. In detail, the construction of heterostructure can achieve the following advantages: (i) high surface area that can enhance reactant/catalyst interactions via increasing adsorption performance toward targeted models; (ii) enhanced separation rates of photoinduced electron-hole resulted from that the formed junction can accelerate charge transfer across the interface and shortens the charge transport distance; (iii) the uniform

distribution of photocatalytically active sites, and (iv) broadening the light spectrum to visible light region. Importantly, the π - π interactions between the massive aromatic rings of organic ligands in MOFs and the triazine rings of g-C₃N₄, along with abundant surface electrostatic interactions, will help them achieve close contact, heterojunction construction as well as effective electron transfer [107,108].

2. The status of g-C₃N₄/MOF binary photocatalysts

Some representative MOFs like ZIF-8, MIL-53, MIL-101, MIL-125, HKUST-1, MOF-5, and UiO-66 exhibited excellent properties and various potential applications [19]. Up to now, several MOFs (ZIF-8, UiO-66, MIL-53, MIL-100, MIL-101, MIL-125, CuBTC, MIL-88B and BUC-21) and g-C₃N₄ with different morphologies (nanosheet, nanorod and nanotube) were combined to construct some binary heterojunction composites (Table 1), which can take advantage of the complementary

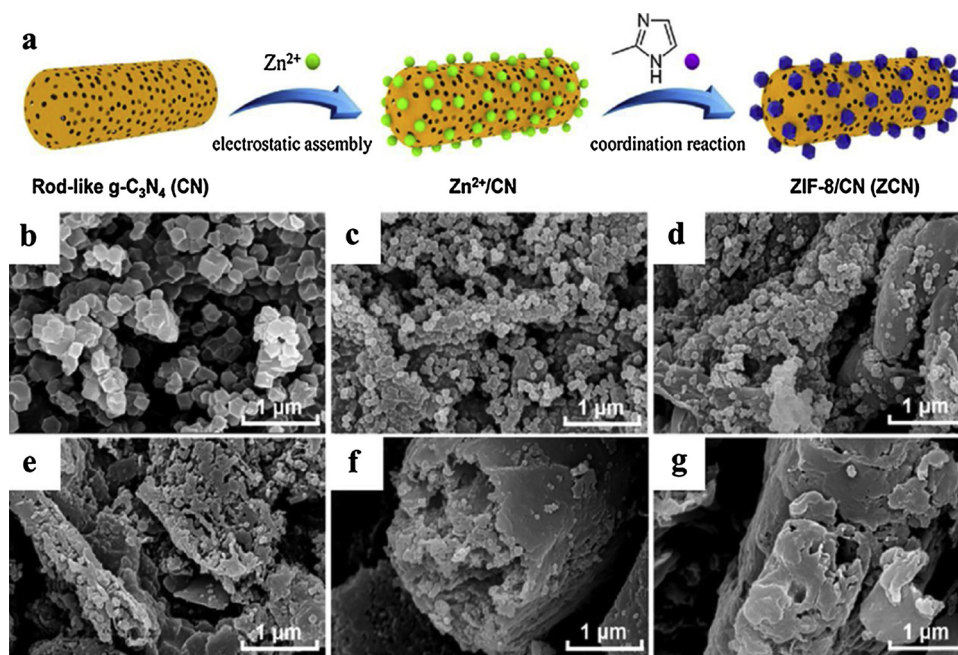


Fig. 3. (a) Schematic diagram of synthesis for ZCN-X composites (ZIF-8/modified rod-like $g\text{-C}_3\text{N}_4$); SEM images of (b) ZIF-8, (c) ZCN100, (d) ZCN200, (e) ZCN400, (f) ZCN800, (g) modified $g\text{-C}_3\text{N}_4$ sample CN [110], copyright (2018) Elsevier.

merits of MOFs and $g\text{-C}_3\text{N}_4$ and overcome their disadvantages. In this section, the heterostructure composites constructed between some MOFs (like ZIF-8, UiO-66(-NH_2), MIL-53(Al/Fe) and MIL-100(Fe)) and $g\text{-C}_3\text{N}_4$ were selected to highlight their fabrication methods, characterizations, photocatalytic performances and mechanism.

2.1. $g\text{-C}_3\text{N}_4/\text{ZIF-8}$

ZIF-8 [$\text{Zn}(\text{2-methylimidazole})_2 \cdot 2\text{H}_2\text{O}$], constructed from 2-methylimidazole organic ligands and Zn^{2+} center ions, exhibits outstanding thermal/chemical stability [127], and large BET specific surface area (SSA) ($\approx 2000 \text{ m}^2/\text{g}$) [128]. ZIF-8 was widely used in various fields including but not limited to gas storage [129,130], separation [131], adsorptive removal of pollutants [132], catalysis [133,134], and sensing [135]. In 2014, ZIF-8 was selected as photocatalyst to conduct MB degradation under UV light irradiation, in which the degradation pathway and mechanism were proposed and verified [30]. Subsequently, some ZIF-8 based photocatalysts like $\text{MoO}_3/\text{ZIF-8}$ [136], $\text{TiO}_2/\text{ZIF-8}$ [137], $\text{Ag/AgCl}/\text{ZIF-8}$ [138,139], $\text{Cd}_{0.5}\text{Zn}_{0.5}\text{S}/\text{ZIF-8}$ [140], $\text{ZnO}/\text{ZIF-8}$ [141] were fabricated to achieve enhanced photocatalytic performances toward CO_2 reduction, Cr(VI) reduction, and organic pollutants degradation.

Recently, ZIF-8 and $g\text{-C}_3\text{N}_4$ with different morphologies were fabricated and composited to combine their both merits, aiming to enhance their photocatalytic performances. Considering that the $g\text{-C}_3\text{N}_4$ nanotube (TCN) thermally prepared via a rolling-up mechanism can accomplish fast photo-response and reproducible photoconductivity [142], suitable amount of transparent ZIF-8 nanocluster [143] was introduced to decorate the well-designed TCN to further increase CO_2 capture and adsorption selectivity without decreasing light absorption capacity [109]. In the powder X-ray diffraction (PXRD) patterns of prepared TCN/ZIF-8 (TCNZx, x is related to the initially designed mass ratio of TCN to ZIF-8) composites, the strong diffraction peak at 27.4° ($d = 0.326 \text{ nm}$) was attributed to the inter-planar stacking of conjugated aromatic systems, corresponding to the (002) plane of both tubular and bulk $g\text{-C}_3\text{N}_4$ [144]. It was worthy to noting that a minor diffraction peak at ca. 17.4° ($d = 0.490 \text{ nm}$) of TCN and ca. 13.0° ($d = 0.681 \text{ nm}$) of bulk $g\text{-C}_3\text{N}_4$ implied that they was built up from the s-triazine based building units and tri-s-triazine based building units,

respectively [74,142]. The noticeable PXRD peaks of ZIF-8 nanoclusters could be detected in the PXRD patterns of TCNZ composites when the content of decorated ZIF-8 was high enough (like TCNZ1), indicating that the ZIF-8 nanocluster could assembly on the surface of TCN without altering its surface. The successful fabrication of the TCNZ composites was further confirmed by their microstructure observed by both filed-emission scanning electron microscopy (FESEM) and transmission electron microscopy (TEM). As illustrated in the Fig. 1, the tubular morphology of TCN was maintained well after the decoration of suitable ZIF-8 nanocluster. As well, most pores of the TCN were filled by ZIF-8 nanocluster, resulting into the smoother surface. It was reported that the thin tubular structure would favor the charge separation and the transportation of reactants/products [145,146]. Also, the reaction pathway and dynamics of the photocatalytic CO_2 reduction were essentially controlled by the adsorption of CO_2 onto the photocatalyst surface [147]. As demonstrated in Fig. 2a and b, the incorporation of ZIF-8 nanocluster into the TCN led to the improved CO_2 adsorption capacity. Furthermore, the CO_2 adsorption capacities of the TCNZ composites increased with the increase of ZIF-8 nanocluster contents. As illustrated in Fig. 2c, the decoration of transparent ZIF-8 nanocluster over the surface of TCN didn't lead to inhabitation of visible light absorption ability. All the conduction band (CB) values facilitate the thermodynamically photocatalytic CO_2 reduction (Fig. 2d), however, taking electrical conductivity (flat band potential) and CB potential into account, the grafted ZIF-8 cluster onto TCN lead to both positive and negative influences toward the photocatalytic performance. According to the in-situ monitor of FTIR (Fig. 2b), the CH_3OH formation from the photocatalytic CO_2 reduction can be described as typical two-electron and two-proton reaction pathway, i.e. ($\text{CO}_2 \rightarrow \text{HCOOH} \rightarrow \text{HCHO} \rightarrow \text{CH}_3\text{OH}$) [148]. As illustrated in Fig. 2e, the photocatalytic CO_2 reduction into CH_3OH can be significantly improved by the combination between TCN and ZIF-8 nanoparticles, in which the CH_3OH production over TCNZ8 is three times higher than that over TCN. Although the CO_2 adsorption capacity increased with the increase of ZIF-8 content into the TCN composites, the surface charge transfer would be inhibited by the increasing introduction of ZIF-8 resulting from its weak electrical conductivity, which was affirmed by the determination of photoluminescence (PL) spectra and transient photocurrent response. In PL spectra as shown in Fig. 2e, the weak emission peak at ca. 400 nm was

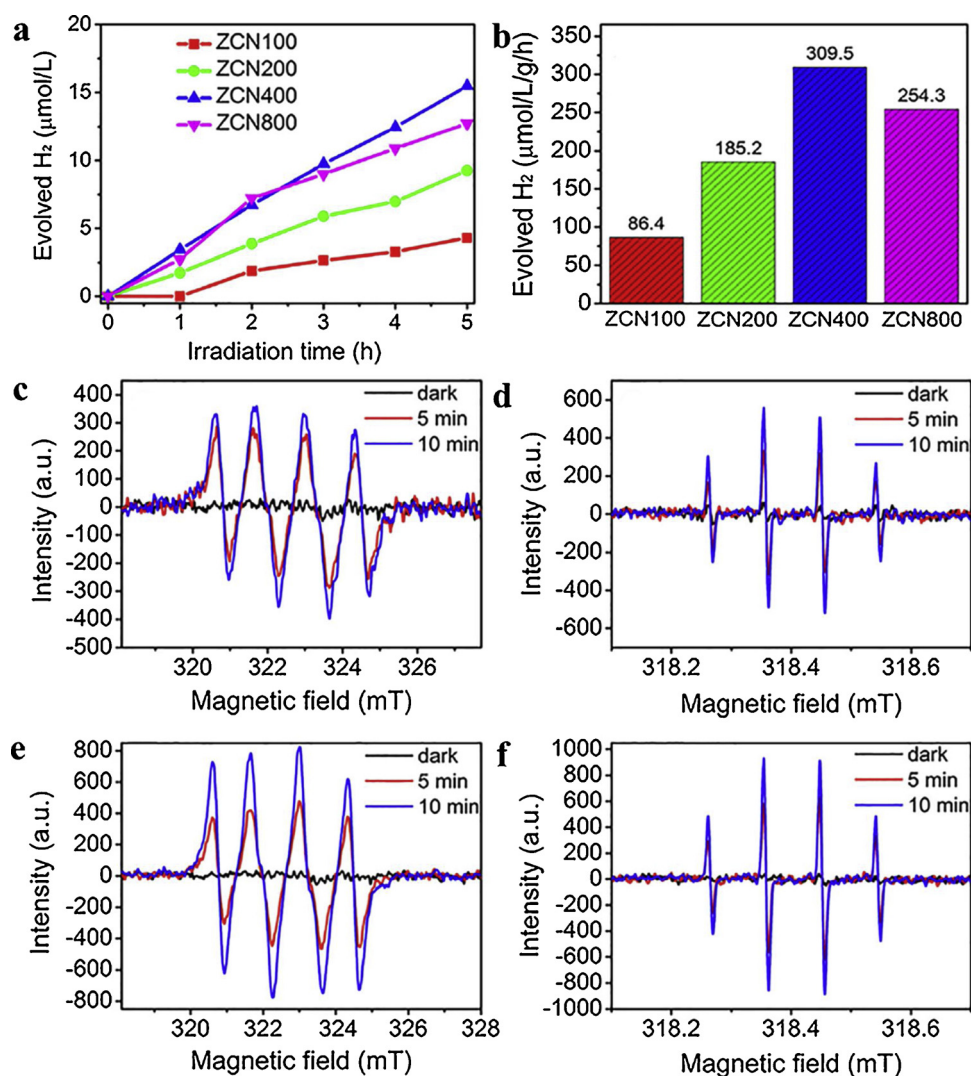


Fig. 4. (a) Solar-driven photocatalytic H₂ evolution activity and (b) H₂-evolving rates; ESR spectra of radicals adducts trapped by DMPO in (c) methanol and (d) aqueous dispersions of CN, along with in (e) methanol and (f) aqueous dispersions of ZCN400 [110], copyright (2018) Elsevier.

assigned to TCN, much different from the strong emission peak at ca. 450 nm of bulk g-C₃N₄ (BCN), which implied that the unique tubular structure favored the charge separation. Noticeably, the determination results of both PL and transient photocurrent response of TCNZ composites revealed that their photocatalytic performance is lower than that of TCN. However, the combination of enhanced adsorption and photocatalysis led to that the TCNZ composite photocatalyst exhibited improved photocatalytic activity for the CO₂ reduction, reaching 0.75 μmol h⁻¹ g⁻¹ under mild reaction condition. Two additional merits of ZIF-8 made it an outstanding candidate for fabricating ZIF-8/g-C₃N₄ heterojunction for photocatalytic CO₂ reduction: (i) the transparency of ZIF-8 will not suppress too much the light harvesting capacity; (ii) the gas adsorption selectivity within ZIF-8 made it can adsorb the reactant CO₂ effectively, but not be affinitive to the reduction products like CH₄ and CH₃OH. This work provides a strategy to fabricate outstanding photocatalysts by combining the merits of semiconductor nanostructure and the surface of MOFs.

Considering the structural merits of g-C₃N₄ and ZIF-8, Xiaofei Yang and coworkers proposed a two-step strategy (electrostatically-driven assembly process and thermal treatment process) to prepare g-C₃N₄/ZIF-8 hybrids (ZCN) via anchoring polyhedral ZIF-8 nanoparticles onto the surface of rod-like g-C₃N₄ [110]. As illustrated in Fig. 3a, the prepared porous rod-like g-C₃N₄ nanorods with negative surface charge (zeta potential being -48 mV) were interacted with Zn²⁺ to form the

intermediates, which were further reacted with 2-methylimidazole to accomplish in-situ fabrication of polyhedral ZIF-8 nanoparticles onto rod-like g-C₃N₄. The successful fabrication of g-C₃N₄/ZIF-8 (ZCN) hybrids was further confirmed by FE-SEM (Fig. 3b–g), powder X-ray diffraction (PXRD) and X-ray photoelectron spectroscopy (XPS).

The ZCN hybrids were further used as photocatalyst to conduct hydrogen evolution from water splitting. As demonstrated in Fig. 4a, the highest hydrogen yield (ca. 15 μmol L⁻¹) and fastest reaction rate were accomplished over ZCN400 (Fig. 4b) with the aid of Pt (wt3%) under visible light irradiation (λ > 420 nm). To clarify the mechanism of the enhanced photocatalytic hydrogen evolution performances over ZCN400, the active radicals formed during the reaction process were determined by electron spin resonance (ESR), in which the 5,5-dimethyl-1-pyrroline-N-oxide (DMPO) was used as the radical scavenger. The results shown in Fig. 4c–f revealed that the signal intensities of active radicals in ZCN400 were almost two times higher than that of pristine rod-like g-C₃N₄. Also, it could be concluded that ·OH was major active specie along with O₂⁻ as minor active radicals to achieve photocatalytic hydrogen evolution from water splitting.

In both TCNZ [109] and ZCN [110] composites, g-C₃N₄ nanotube and rod-like g-C₃N₄ were fabricated as substrates to deposit ZIF-8 nanoparticles, while Hareesh and coworkers developed an in-situ generation method to anchor C₃N₄ nanosheets over ZIF-8 nanocrystals to fabricate micro-mesoporous structures (ZC) [111]. As depicted in

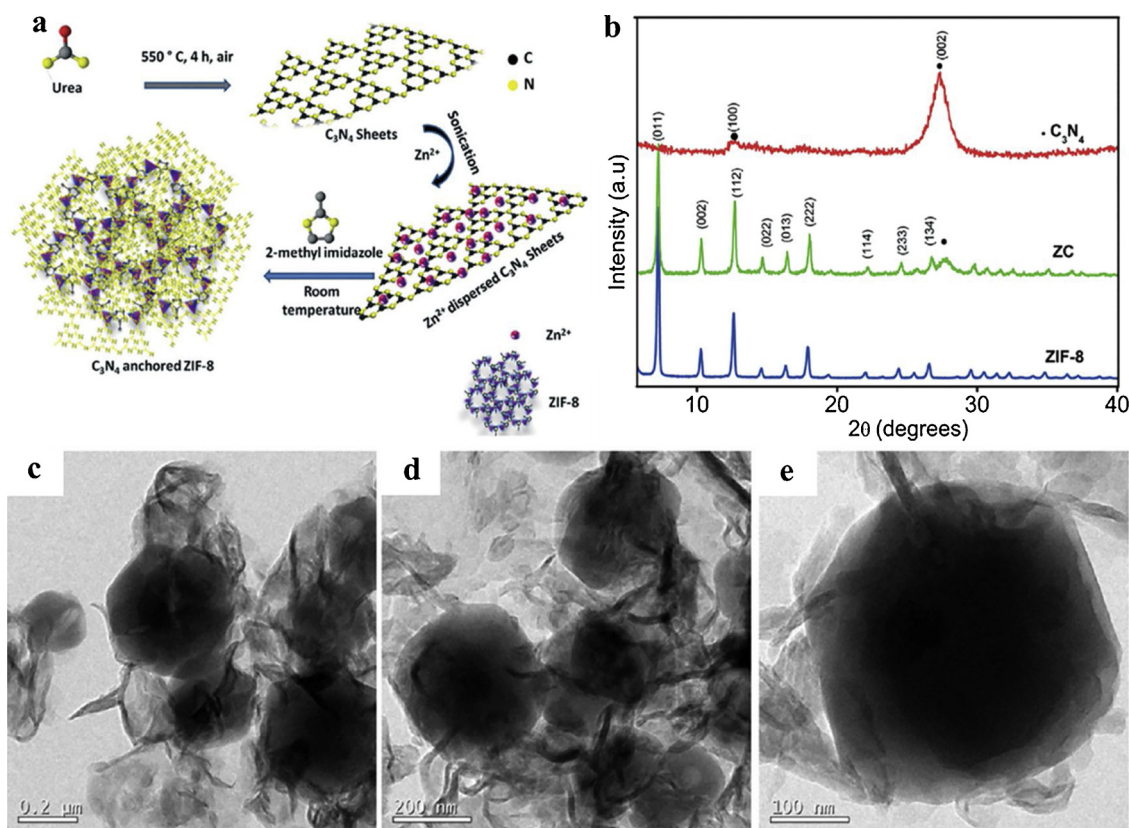


Fig. 5. (a) Schematic diagram of the C₃N₄-ZIF-8 (ZC) composites; (b) PXRD patterns of the as-prepared g-C₃N₄, ZIF-8, and ZC composite (peaks marked • represent C₃N₄ phases, and the remaining peaks belong to ZIF-8); (c) TEM of C₃N₄-ZIF-8 (ZC); (d) and (e) Magnified TEM images of TEM of ZC [111], copyright (2017) Royal Society of Chemistry.

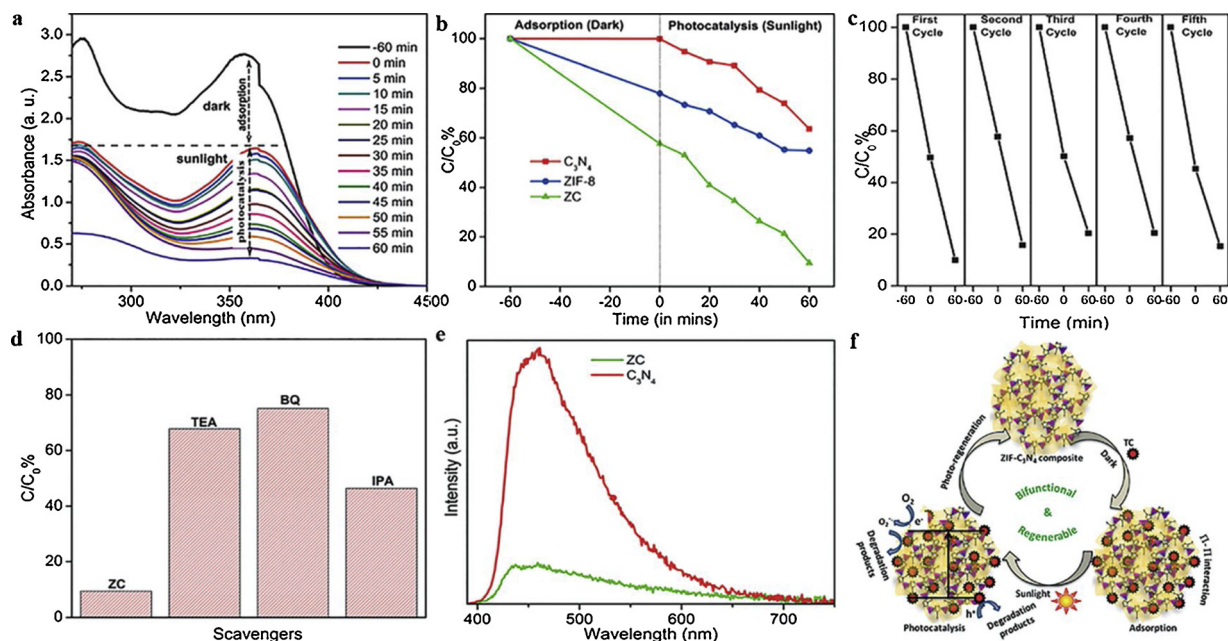


Fig. 6. (a) The UV spectra of TC during the adsorption and degradation stages using C₃N₄-ZIF-8 (ZC) composite; (b) Photocatalytic degradation profile of TC using g-C₃N₄, ZIF-8, and ZC composite; (c) The repetitive adsorption and photocatalytic degradation cycles of ZC composite; (d) Photocatalytic degradation of TC using ZC composite with ROS scavengers IPA, TEA, BQ and pure ZC; (e) Photoluminescence spectrum of g-C₃N₄ and ZC composite; (f) Schematic illustrating the adsorption and photocatalytic degradation mechanisms of tetracycline by ZC composite [111], copyright (2017) Royal Society of Chemistry.

Table 2

The zeta potential of ZC, the interactions between ZC composite and TC species [111].

pH	Zeta potential of ZC (mV)	Surface charge of TC at this pH value	TC species	Dominant interaction in adsorption
2	6.7	Positive	TCH_3^+	Electrostatic repulsion
4	5.4	Neutral	TCH_2	π - π interaction and electrostatic attraction
6	-25	Neutral	TCH_2	π - π interaction and electrostatic attraction
8	-29	Negative	TCH^-	π - π interaction and electrostatic attraction
10	-29	Negative	TC^{2-}	Electrostatic repulsion
	-55	Negative	TC^{2-}	Electrostatic repulsion

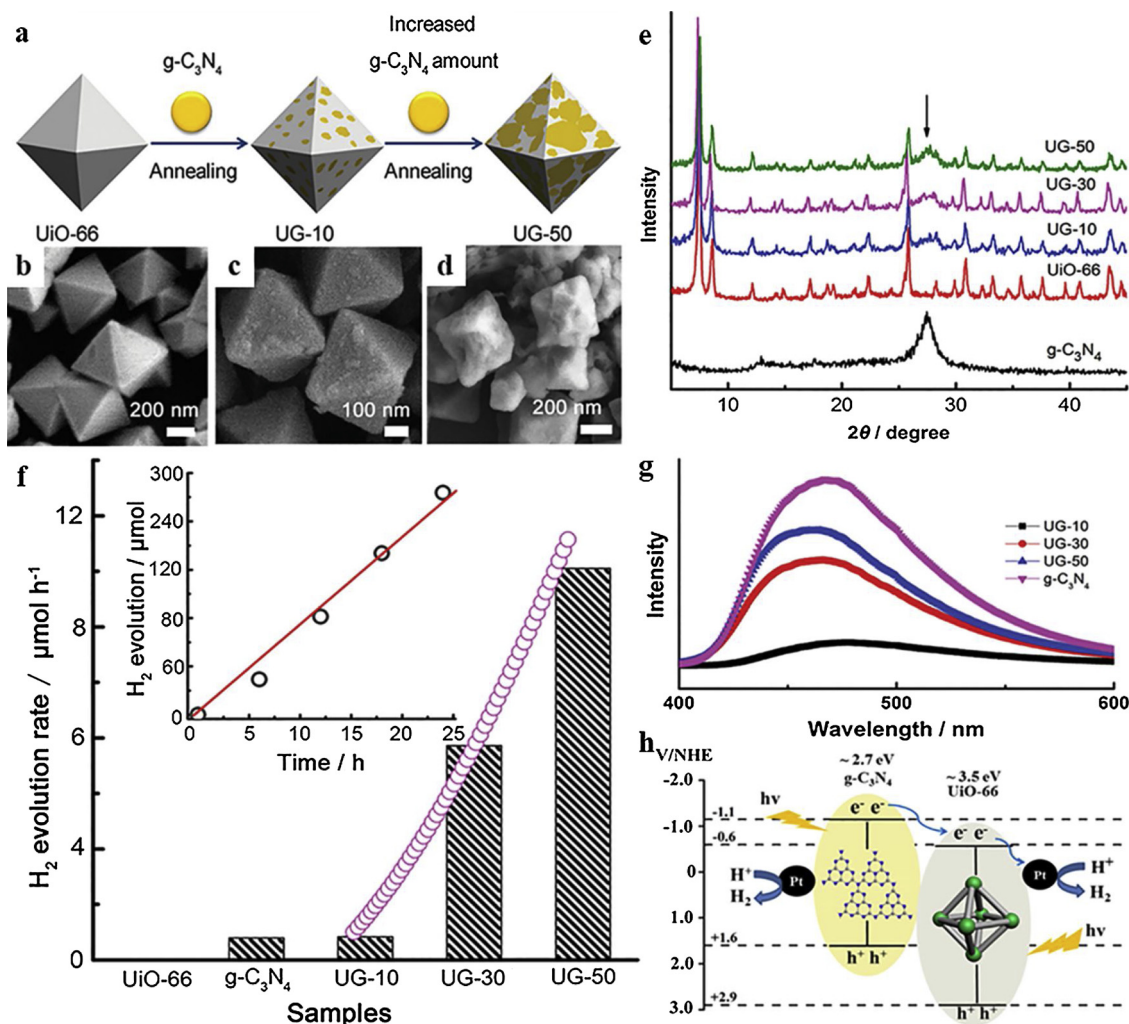


Fig. 7. (a) Schematic illustration of decorating g-C₃N₄ on UiO-66 octahedrons via annealing process. Increasing the g-C₃N₄ amount leads to higher coverage of g-C₃N₄ on UiO-66 octahedrons; SEM images of (b) UiO-66, (c) UG-10 and (d) UG-50; (e) XRD patterns of g-C₃N₄, UiO-66, UG-10, UG-30, and UG-50 hybrid photocatalysts; (f) The histogram showing the H₂ production rate over UG-x samples (x = 10, 30, and 50). The H₂ production rate is taken from the first 4 h photocatalytic reaction. The H₂ production rate over pristine UiO-66 and g-C₃N₄ was also included for comparison. The inset shows the long term H₂ production over UG-50 sample; (g) The stable state PL spectra of UG-x (x = 10, 30, and 50); (h) The schematic illustration of possible mechanism [107], copyright (2015) Wiley.

Fig. 5a, the C₃N₄ with surface area of 132 m² g⁻¹ was prepared by thermal decomposition of urea at 550 °C; And then, the as-prepared C₃N₄ was suspended in zinc nitrate aqueous solution by ultrasonication; Finally, the C₃N₄/ZIF-8 (ZC) was fabricated after 2-methylimidazole was added to the suspended solution at 30 °C. As illustrated in Fig. 5b, the PXRD patterns of ZC displayed the characteristic peaks of g-C₃N₄ and ZIF-8, implying the successful formation of C₃N₄/ZIF-8 hybrids. It was interesting to find that the (002) peak of C₃N₄ in ZC composite shifted slightly being compared to pristine C₃N₄, which can be assigned to that the ZIF-8 nanocrystals were wrapped by C₃N₄ sheets. The TEM images as demonstrated in Fig. 5c–e confirmed that the ZIF-8 nanocrystals were wrapped efficiently by exfoliated C₃N₄ nanosheets, which

provided rapid interfacial charge transfer between ZIF-8 and C₃N₄ nanosheets to facilitate the photocatalytic reaction [149,150].

The pristine C₃N₄ exhibited nearly no adsorption activity towards tetracycline (TC), and displayed weak photocatalytic degradation performances toward TC (30%, with initial TC concentration being 200 μM) under the visible light irradiation for 120 min (Fig. 6b), due to its small surface area and fast recombination of photo-induced electron and hole. It was worthy to noting that ZC composite can achieve 45% adsorption (maximum adsorption capacity being 382 mg g⁻¹) along with 90% degradation efficiency toward TC within 120 min under sunlight irradiation. The enhanced adsorption performance of ZC toward TC can be contributed to the improved surface area, micro-

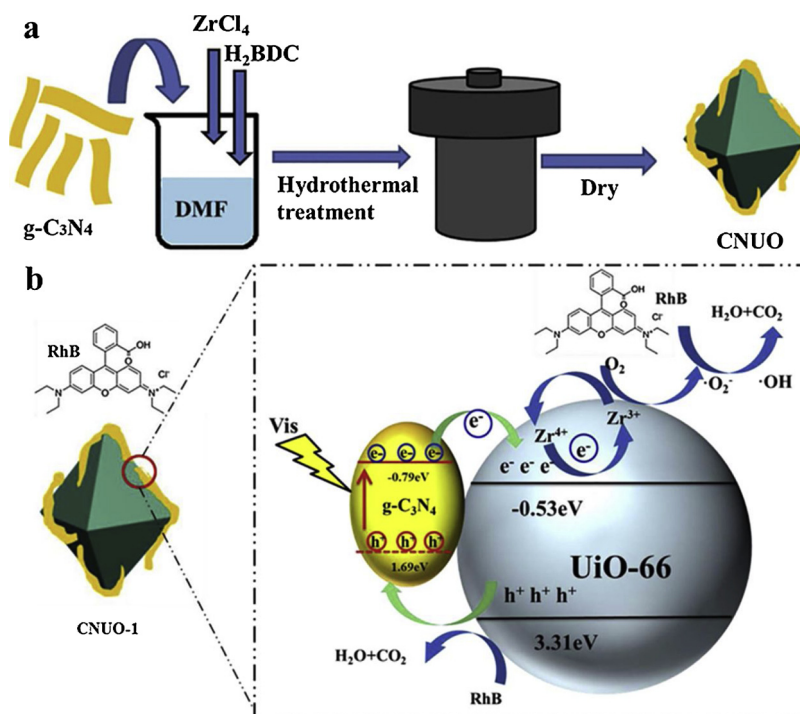


Fig. 8. (a) A schematic illustration of oxidation of dye over CNUO-1 nanocomposite under visible light irradiation; (b) A schematic illustration of oxidation of dye over CNUO-1 nanocomposite under visible light irradiation [113], copyright (2018) Elsevier.

mesoporous structure and powerful π - π stacking interactions between TC species and ZC composite (as listed in Table 2). It was found in Fig. 6a that the maximum absorption peak at 357 nm of TC was slightly moved to 364 nm, which might result from the strong interactions between TC and ZC composites [151].

To clarify the possible mechanism of ZC composite's photocatalytic reaction, the reactive species (RS) trapping experiments along with the photoluminescence determination were carried out. Trithanolamine (TEA), benzoquinone (BQ) and isopropyl alcohol (IPA) were used as scavengers to capture holes, superoxide anions and hydroxyl radicals, respectively. As illustrated in Fig. 6d, the photocatalytic degradation performances were inhibited significantly with the addition of these three scavengers, following the order of BQ > TEA > IPA. In order to investigate the recombination rate of photo-produced holes and electrons, the photoluminescences (PL) of C_3N_4 and ZC composite were detected, in which the PL emission intensity of ZC at 460 nm due to band-band stacking of C_3N_4 decreased significantly, comparing to the individual C_3N_4 (Fig. 6e). In all, the micro-mesopore structure of ZC composite facilitated their enhanced adsorption and photocatalytic performances due to that they provided adequate active sites. The schematic illustration of the adsorption and photocatalytic degradation mechanisms of C_3N_4 -ZIF-8 (ZC) composite toward tetracycline was depicted in Fig. 6f. Upon the irradiation of sunlight, the excited electrons in the lowest unoccupied molecular orbital (LUMO) (-3.41 eV) of ZIF-8 are transferred to the relatively low CB (-1.32 eV) of C_3N_4 , which react with O_2 to form superoxide radicals ($\cdot O_2^-$) to further degrade TC molecules. Also, the holes in the highest occupied molecular orbital (HOMO) (1.68 eV) of ZIF-8 decompose the TC molecules directly without transporting to the VB (1.62 eV) of C_3N_4 due to their close VB potentials. Due to the synergy effect between these two constitutes, the recombination between the excited holes and electrons is inhibited, and the photocatalytic ability is improved. This bifunctional C_3N_4 /ZIF-8 composite with adsorption and photocatalysis activities provides a good solution to achieve efficient removal of pollutants like tetracycline without the input of additional energy/chemicals and free of secondary treatment. Generally, the adsorption is a spontaneous process, hence desorption is achieved with the aid of chemical or energy input [10]. In

this work, the ZC composite as adsorbent could be regenerated by photocatalytic degradation toward TC, which provided a new strategy to achieve re-generality of adsorbents. Also, ZC composite is stable and can be reused for long time, which can be affirmed by five runs' recyclability (Fig. 6c).

2.2. $g-C_3N_4$ /UiO-66

UiO-66 is constructed from $Zr_6O_4(OH)_4$ octahedra linked by 1,4-benzene-dicarboxylate (BDC) linker, which possessed very high surface area (1147 m²/g) and ultrahigh thermal stability and chemical stability resulted from their strong Zr-O bond and high coordination number of Zr(IV) [152–156]. Considering its merits like exceptional porosity, high internal surface area and the active Zr-O cluster, UiO-66 had been widely used in various research fields like catalysis [157,158], photocatalysis [159–164], gas adsorption & separation [165–169], adsorptive removal of organic pollutants in wastewater [170]. The photocatalytic activities of UiO-66 and UiO-66-NH₂ were firstly reported to accomplish H₂ production from methanol or the mixture of methanol/H₂O upon the irradiation of 300 nm light [161]. Recently, Li et al. reviewed the argument of the UiO-66-NH₂'s photocatalytic activity origin [164]. Considering the finding of ESR signal corresponding to Zr^{3+} , Li and coworkers along with Long and coworkers believed that the photo-induced Zr^{3+} generated via ligand-metal-charge-transfer (LMCT) resulted into the UiO-66-NH₂'s excellent photocatalytic performance [159,162]. While, Matsuoka and coworkers as well as Gascon and coworkers insisted that no Zr^{3+} can be produced in UiO-66-NH₂ due to the highly negative redox potential of Zr-O clusters [171] and purely ligand-based highest occupied crystal orbital (HOCO) - lowest unoccupied crystal orbital (LUCO) transition [172]. Although further studies are urgently needed to clarify the pending debate on the origin of UiO-66-NH₂'s photocatalytic activity, more and more researchers introduced it into their photocatalysis system to achieve appealing photocatalytic performance.

Considering that both UiO-66 and $g-C_3N_4$ displayed limited photocatalytic performances due to their quick charge recombination and restricted light adsorption ability [159–164,172,173], Yuan and

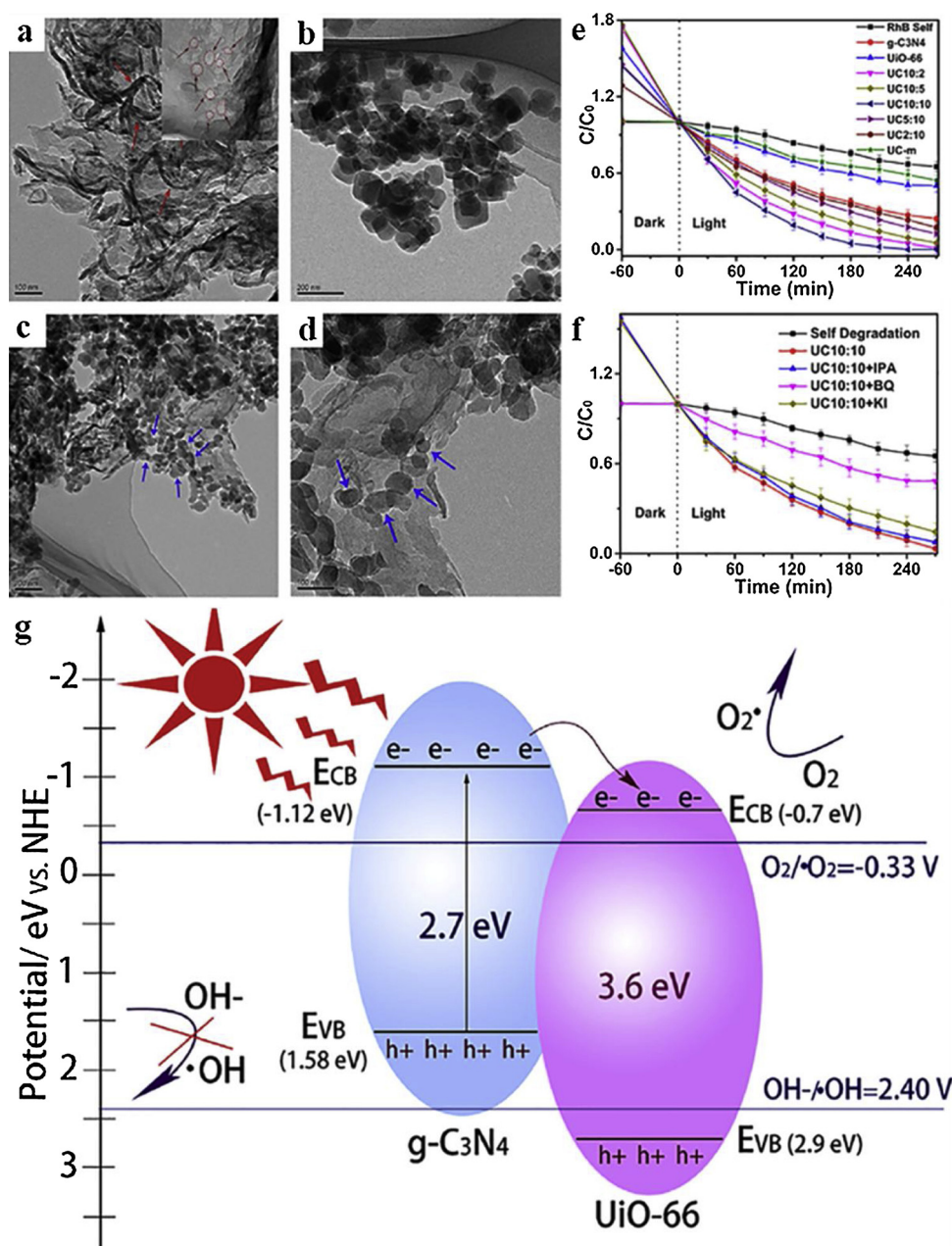


Fig. 9. TEM images of (a) g-C₃N₄ nanosheets, (b) UiO-66 octahedrons, (c) and (d) UC10:10 heterojunctions hybrids; (e) Photocatalytic activity of UiO-66, g-C₃N₄ nanosheets and UC x:y hybrids for the degradation of MB under visible light; (f) Effects of different scavenger addition in the photocatalytic degradation of MB under visible light; (g) Proposed mechanism of photocatalytic degradation of MB by the UiO-66/g-C₃N₄ heterojunction photocatalyst under visible light irradiation [114], copyright (2018) Elsevier.

coworkers developed quasi-polymeric g-C₃N₄/UiO-66 hybrids (UG-x, x = the mass ratio of g-C₃N₄ in the hybrids) to achieve enhanced photocatalytic hydrogen production via water splitting [107]. As illustrated in Fig. 7a, the UG-x hybrids were prepared via annealing the matrix of UiO-66 and g-C₃N₄ with different mass ratio in argon atmosphere. The PXRD, SEM, TEM and HR-TEM confirmed the formation of g-C₃N₄/UiO-66 hybrids, in which the clear interface between g-C₃N₄ and UiO-66 facilitated the rapid charge transfer between these two components (Fig. 7a–e). The UG-X hybrids demonstrated enhanced photocatalytic H₂ production under the conditions of ascorbic acid (0.1 M, pH = 4) as scavenger and Pt as co-catalyst upon visible light illumination, in which the H₂ production ratios of UG-10 and UG-50 were 11 and 17 times higher than that of individual g-C₃N₄. However, the excessive g-C₃N₄ into hybrid could result into declined H₂ production rate due to “covering effect”. The UG-x composite (like UG-50) was stable to

accomplish long-term and efficient H₂ production for 24 h (Fig. 7f). The steady-state photoluminescence (PL) determination revealed that the introduction of UiO-66 led to the PL emission (ca. 460 nm of g-C₃N₄) quench, as shown in Fig. 7g, implying a rapid charge transfer over UG-x hybrids. It was further affirmed by the decreasing lifetime of charge carrier with the increase amount of UiO-66 (2.88 ns for g-C₃N₄ and 2.26 ns for UG-50). The energy position of CB edge of g-C₃N₄ (-1.1 V vs NHE at pH = 7.0) was more negative than that of UiO-66 (-0.6 V vs NHE at pH = 7.0), resulting into that visible-light-induced electrons in g-C₃N₄ transferred to UiO-66 across the interfaces between these two components. With the aid of Pt particles, the accumulated electrons in g-C₃N₄ and UiO-66 reduced the H⁺ into H₂, and the ascorbic acid consumed the holes in g-C₃N₄ to enhance the photocatalytic H₂ production, as illustrated in Fig. 7h.

Liu and coworkers developed a facile solvothermal method (Fig. 8a)

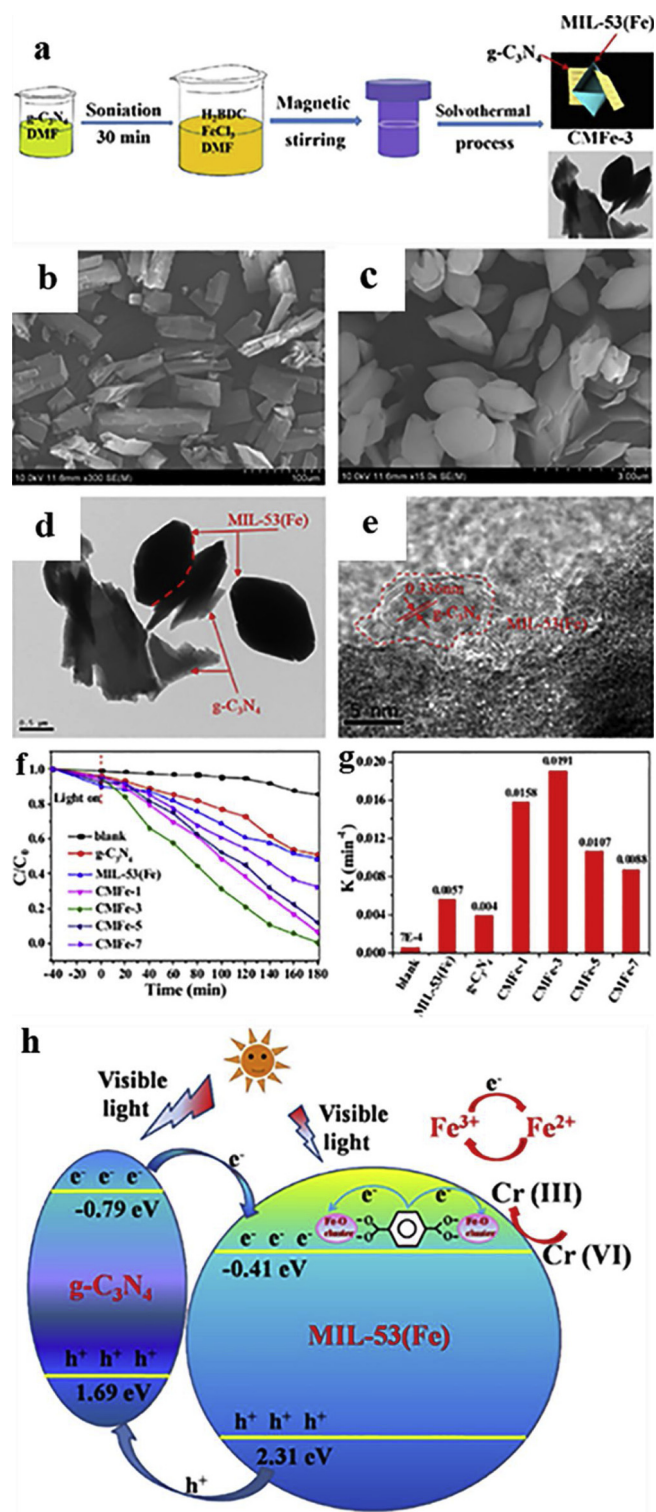
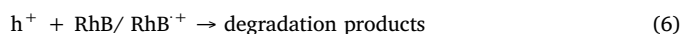
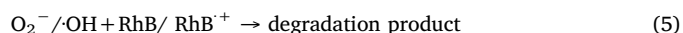
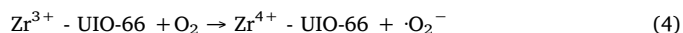
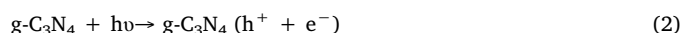


Fig. 10. (a) Schematic illustration for the synthesis of the g-C₃N₄/MIL-53 (CMFe-x) nanocomposite; SEM images of MIL-53 (b), CMFe-3 (c) and TEM (d) and HRTEM (e) images of CMFe-3; Photocatalytic reduction curves (f) of the Cr (VI) (pH = 3) and the apparent reaction rate constants of Cr(VI) (g) using different photocatalysts after 180 min of visible light irradiation; (h) Schematic illustration of the reduction of Cr(VI) over CMFe-3 nanocomposite under visible light irradiation [9], copyright (2017) Elsevier.

to fabricate g-C₃N₄/UiO-66 nanohybrids (CNUO-x) [113], which were used to conduct enhanced photocatalytic RhB degradation under visible light irradiation. This work highlighted the possible photocatalytic mechanism of CNUO-x (like CNUO-1) toward RhB degradation, as

illustrated in Fig. 8b. (i) The adsorbed H₂O can be oxidized into ·OH radicals by photo-generated holes, due to that the VB of UiO-66 (+3.31 eV vs NHE) is more positive than the standard electrode potential of ·OH/H₂O (+2.4 eV vs NHE). (ii) The photo-generated holes on CB of g-C₃N₄ (-0.79 eV vs NHE) are transferred to the CB of UiO-66 (-0.53 eV vs NHE), which inhibited the recombination of photo-generated holes/electrons to enhance the photocatalytic activities. (iii) The photo-generated electrons on VB of UiO-66 can reduce O₂ into ·O₂⁻ radicals. (iv) The RhB molecules adsorbed on the surface of CNUO-1 upon the irradiation of visible light can be excited to form RhB*, which can be degraded by active species like h⁺, ·O₂⁻ or ·OH. The electrons from RhB and g-C₃N₄ can reduce Zr⁴⁺ in the Zr-O cluster of UiO-66 into Zr³⁺, and the Zr³⁺ can be oxidized to Zr⁴⁺ [174]. Hence, h⁺, ·O₂⁻ or ·OH can decompose RhB and RhB*, following the Reactions (1)–(6).



Zou et al. prepared UiO-66/g-C₃N₄ heterojunction UC x:y (x:y = 2:10, 5:10, 10:10, 10:5 and 10:2, corresponding to the added amount of g-C₃N₄ being 83.3, 66.7, 50.0, 33.3, and 16.7 wt%) photocatalyst via a facile annealing the matrix of UiO-66 and g-C₃N₄ nanosheet [114], which was affirmed by TEM, XRD, XPS, TG-DSC, UV-vis DRS, PL and BET. The TEM images shown in Fig. 9a–d revealed that the as-prepared g-C₃N₄ nanosheet is thin and flat, in which some in-plane holes with size ranging 60–90 nm contributed the increasing specific surface area. The UiO-66 octahedrons were coated on the g-C₃N₄ sheets after annealing at 350 °C for 2 h in air atmosphere, and both UiO-66 and g-C₃N₄ were stable to keep their morphology structures during the annealing process. The photocatalytic degradation performances of UiO-66/g-C₃N₄ heterojunction UC x:y toward MB under the irradiation of visible light was displayed in Fig. 9e. It was found that UC 10:10 could achieve best photocatalytic degradation performance, which resulted from the UiO-66's internal porous structure to facilitate the adsorption of MB and the formed heterojunction to inhibit the recombination of photo-generated holes/electrons. In this work, TOC was determined to test the mineralization of MB using UC-10:10 as photocatalyst. The results revealed that 72% TOC removal was accomplished after 240 min illumination. The ·O₂⁻ radicals were identified as the main reactive species to decompose MB, which was affirmed by both the trapping experiment of adding different scavengers and ESR determination. Due to that the inner electronic field formed between the two components in UiO-66/g-C₃N₄ heterojunction, along with more negative conduction band potential of g-C₃N₄ (-1.12 eV vs NHE) than UiO-66 (-0.7 eV vs NHE), the electrons on the CB of g-C₃N₄ were easily moved to the CB of UiO-66, which were captured by the absorbed O₂ to produce ·O₂⁻ radicals and to further decompose the MB molecules (Fig. 9f). In the UiO-66/g-C₃N₄ heterojunctions, UiO-66 acted as a ferry to separate the photogenerated electrons back to the CB of g-C₃N₄, enhancing the photocatalytic degradation activity toward organic dye molecules (Fig. 9g).

2.3. g-C₃N₄/MIL-53

MIL-53 of nanoporous metal-benzenedicarboxylate M(OH)(O₂C-C₆H₄-CO₂) containing Cr³⁺, Al³⁺ or Fe³⁺ as templates [175] can be labeled as MIL-53(Cr) (BET surface area ≈ 1100 m²/g, Langmuir surface area was estimated to be over 1500 m²/g) [176], MIL-53(Al) (with pores of 8.5 Å, BET surface area ≈ 1100 m²/g, Langmuir surface area of 1590 m²/g) and MIL-53(Fe) (BET surface area ≈ 1100 m²/g),

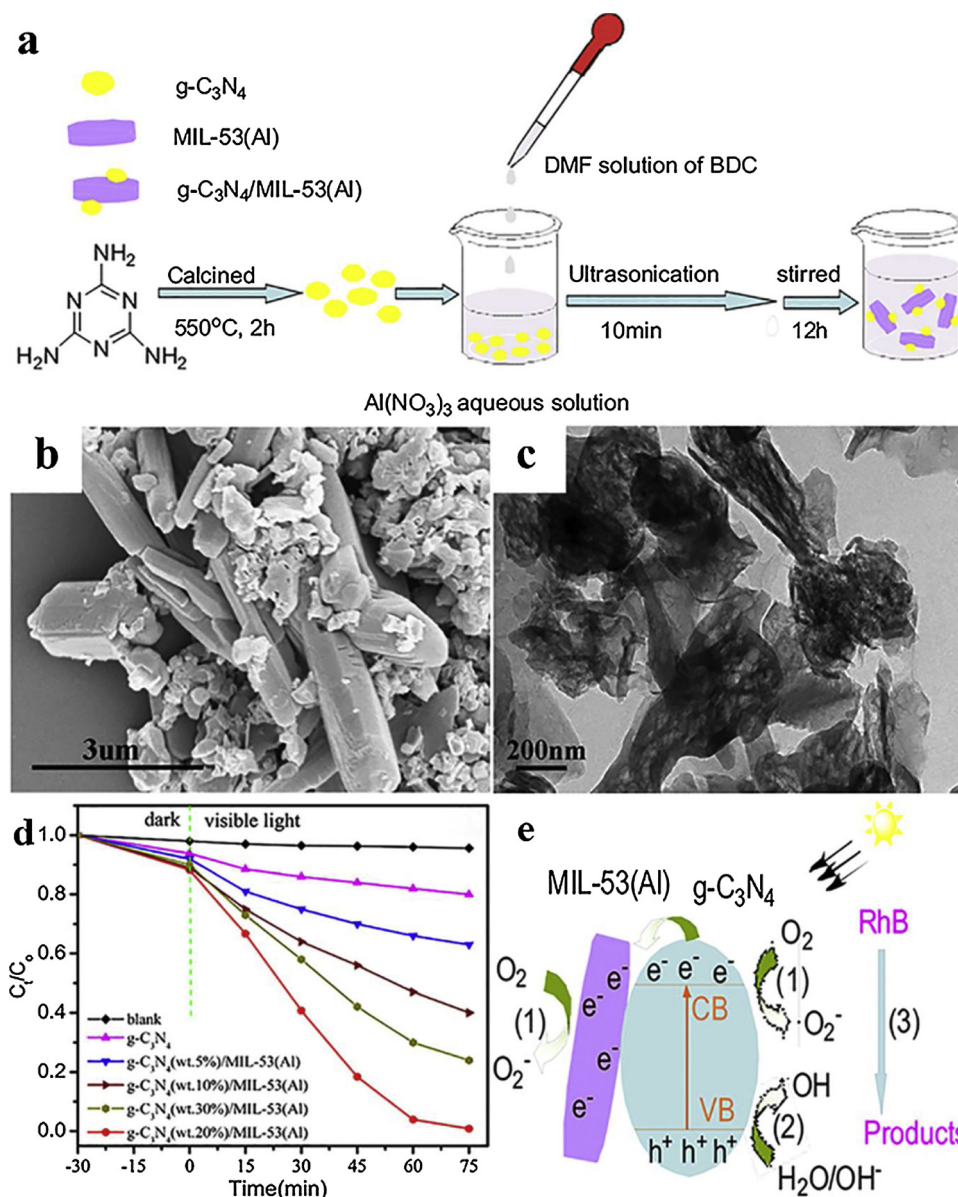
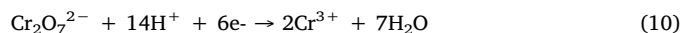
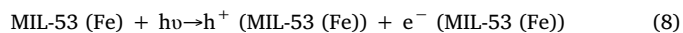
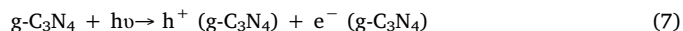


Fig. 11. (a) Fabrication scheme of the g-C₃N₄/MIL-53(Al) composite; (b) SEM images of g-C₃N₄(20 wt%)/MIL-53(Al); (c) TEM image of g-C₃N₄(20 wt%)/MIL-53(Al); (d) Photocatalytic activities of as-prepared g-C₃N₄(x wt%)/MIL-53(Al) photocatalysts for RhB degradation under visible-light irradiation; (e) Mechanism for photodegradation of RhB over g-C₃N₄/MIL-53 (Al) composite under visible-light irradiation [115], copyright (2015) Wiley.

respectively. MIL-53(Fe/Cr/Al) were widely used in the fields of adsorption [177–184], catalysis [185], separation [186,187], sensor [188] and photocatalysis [189–193].

Zhang et al. developed a facile solvothermal method (Fig. 10a) to fabricate g-C₃N₄/MIL-53(Fe) (CMFe-*x*, *x* is the weight content of g-C₃N₄ in the composite), which was confirmed by XRD, FTIR, SEM, TEM, HRTEM and BET [9]. The SEM and TEM images (Fig. 10b–e) demonstrated that g-C₃N₄ with various shapes were coated on the MIL-53(Fe) polyhedrons. Especially, the HRTEM revealed that the fringe spacing of 0.336 nm was assigned to (002) crystal planes of g-C₃N₄. It could be observed that g-C₃N₄ was successfully embedded onto the surface of MIL-53(Fe) to produce heterojunction structure, which could be expected to improve the transfer efficiency of photogenerated electrons. As displayed in Fig. 10f and g, the photocatalytic activities of CMFe-*x* toward Cr(VI) reduction into Cr(III) under visible-light illumination were evaluated. The results revealed that CMFe-3 displayed best photocatalytic Cr(VI) reduction performance with reaction rate of 0.0191 (3.4 and 4.8 times higher than that of individual MIL-53(Fe) and g-

C₃N₄). As illustrated in Fig. 10h, the e⁻ from the CB of g-C₃N₄ was transferred to the CB of MIL-53(Fe), moreover, the h⁺ from the VB of MIL-53(Fe) was moved to the VB of g-C₃N₄, which can reduce the charge recombination and collect more free electrons in the CB of MIL-53(Fe). The involved reactions were listed as Eqs. (7)–(10).



Guo et al. prepared g-C₃N₄/MIL-53(Al) composite via an easy stirring method under room temperature, as illustrated in Fig. 11a [115], in which the content of g-C₃N₄ contents in the composite were calculated by N contents determined by N element analysis. The composite process exerted no obvious change on structure of g-C₃N₄ and MIL-53(Al). The PXRD patterns revealed that after being composited, the

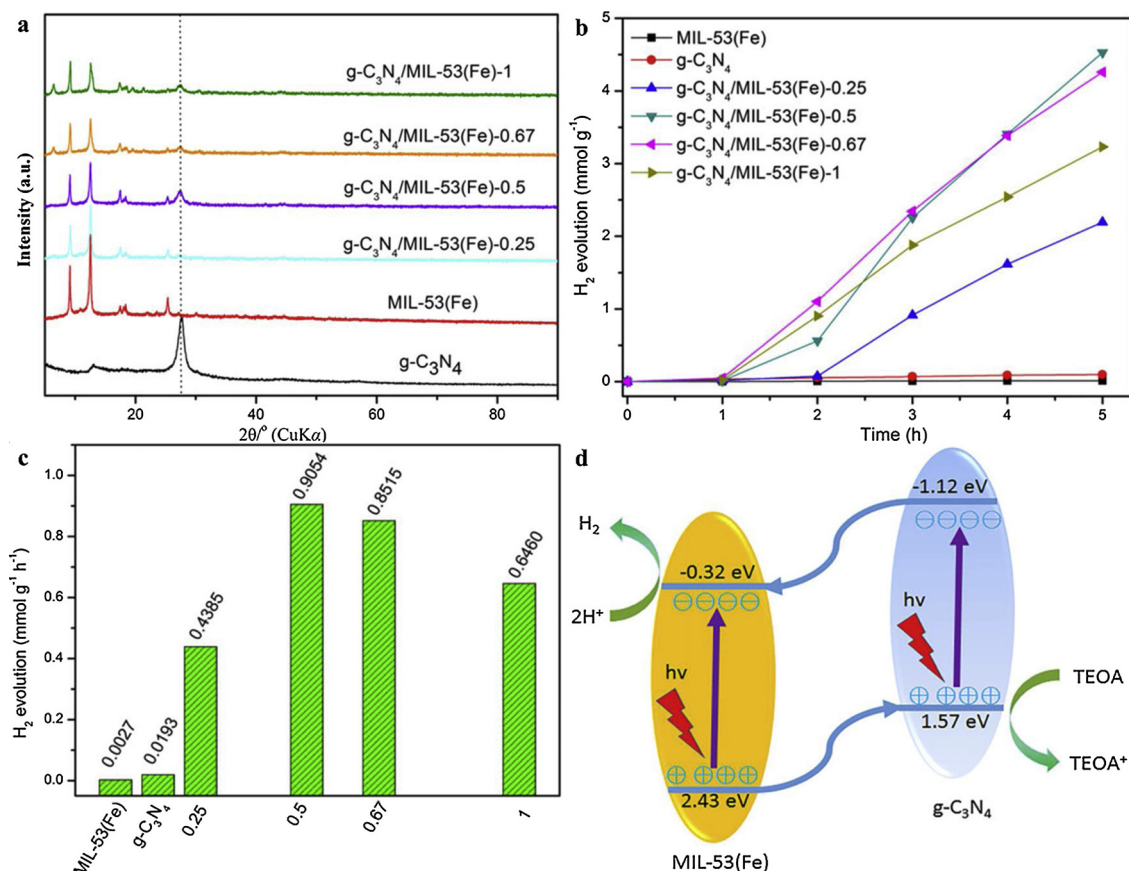


Fig. 12. (a) XRD patterns of g-C₃N₄, MIL-53(Fe) and g-C₃N₄/MIL-53(Fe) composites; (b) H₂ evolution rate of g-C₃N₄/MIL-53(Fe) photocatalysts under visible light irradiation; (c) Comparison of the activities of g-C₃N₄/MIL-53(Fe) photocatalysts for H₂ evolution; (d) Schematic of the possible mechanism for H₂ evolution using the g-C₃N₄/MIL-53(Fe) composite [116], copyright (2018) Wiley.

characteristic peak positions of g-C₃N₄ and MIL-53(Al) maintained well, however, the intensity g-C₃N₄/MIL-53(Al) composites decreased significantly due to their low crystallinity and minor crystal particles. The minor size of MIL-53(Al) particles was confirmed by both SEM and TEM, in which the aggregation of MIL-53(Al) particles significantly decreased with the aid of g-C₃N₄ (Fig. 11b and c). The UV–vis DRS determination exhibited that g-C₃N₄ (20 wt%)/MIL-53(Al) absorption edge was calculated at 540 nm with band gap energy of ca. 2.64 eV, implying that g-C₃N₄ was incorporated into the lattice of MIL-53(Al). Also, the PL spectrum revealed that the PL emission intensity of the g-C₃N₄ (20 wt%)/MIL-53(Al) was weaker than that of pristine MIL-53(Al) and g-C₃N₄, indicating that the introduction of g-C₃N₄ resulted in declined recombination of photogenerated electrons and holes. As a result, the optimal g-C₃N₄ (20 wt%)/MIL-53(Al) composite can achieve nearly 100% RhB decomposition under visible light within 75 min (Fig. 11d), in which $\cdot\text{O}_2^-$ played a major role to degrade RhB along with the h^+ and $\cdot\text{OH}$ as minor active species (Fig. 11e).

Han and coworkers fabricated g-C₃N₄/MIL-53(Fe) hybrids using facile grinding method [116]. The PXRD patterns demonstrated the successful fabrication of g-C₃N₄/MIL-53(Fe) composite, in which the characteristic peaks of both MIL-53(Fe) and g-C₃N₄ were observed significantly (Fig. 12a). The g-C₃N₄/MIL-53(Fe) composites were used as photocatalysts to produce H₂ under simulated sunlight illumination, in which it could be found that the H₂ production rate increased with the introduction of g-C₃N₄ (Fig. 12b). The H₂ production rate of optimum g-C₃N₄/MIL-53(Fe)-0.5 was 0.9054 mmol g⁻¹ h⁻¹, 335 and 47 times higher than that of individual MIL-53(Fe) and g-C₃N₄, respectively (Fig. 12c). The enhanced photocatalytic H₂ production over g-C₃N₄/MIL-53(Fe) composite could be contributed to the following three reasons. (i) Grinding might not only construct effective interfacial

contact between two components, but also provide more active sites to achieve photocatalytic reaction. (ii) Upon the illumination of simulated sunlight, the photogenerated e⁻ in CB of g-C₃N₄ could be migrated easily to the CB of MIL-53(Fe) under the electric field of the composite to inhibit the combination of photogenerated e⁻ and h⁺. (iii) The Fe-oxo clusters in MIL-53(Fe) could play a role of electron acceptor to capture e⁻ with the aid of the transformation from Fe³⁺ to Fe²⁺. In the presence of TEOA as electron donor, photocatalytic H₂ production could be achieved continuously due to the stronger reducing ability of Fe²⁺ in MIL-53(Fe), as illustrated in Fig. 12d.

2.4. g-C₃N₄/MIL-100

Among various MOFs, Fe-based MOFs exhibited great potential as the efficient photocatalysts due to their high chemical stability, non-toxic, low cost along with good photosensitivity [58,194–196], which been applied in a variety of photocatalytic organic transformations [39,53,54,56]. As well, the Fe-based MOFs can accomplish powerful Fenton-like excitation of H₂O₂ for photocatalytic reaction in water treatment and benzene hydroxylation under light irradiation [53,124,190,197,198]. MIL-100(Fe), an iron(III) carboxylate, possesses a large accessible and permanent porosity, which has already been used to conduct the adsorption [199], photocatalytic degradation of organic pollutants [200] and reduction of Cr(VI) [201]. To exploit the complementary features of MIL-100(Fe) and g-C₃N₄ and to inhibit the electron–hole recombination, Petit and coworkers developed an in situ method to produce carbon nitride nanosheets g-C₃N₄/MIL-100(Fe) heterojunction with enhanced photocatalytic performance [118]. The fabrication procedure of CNNs-MIL-x nanocomposites was illustrated in Fig. 13a. Firstly, yellow carbon nitride powder (CN) was prepared from

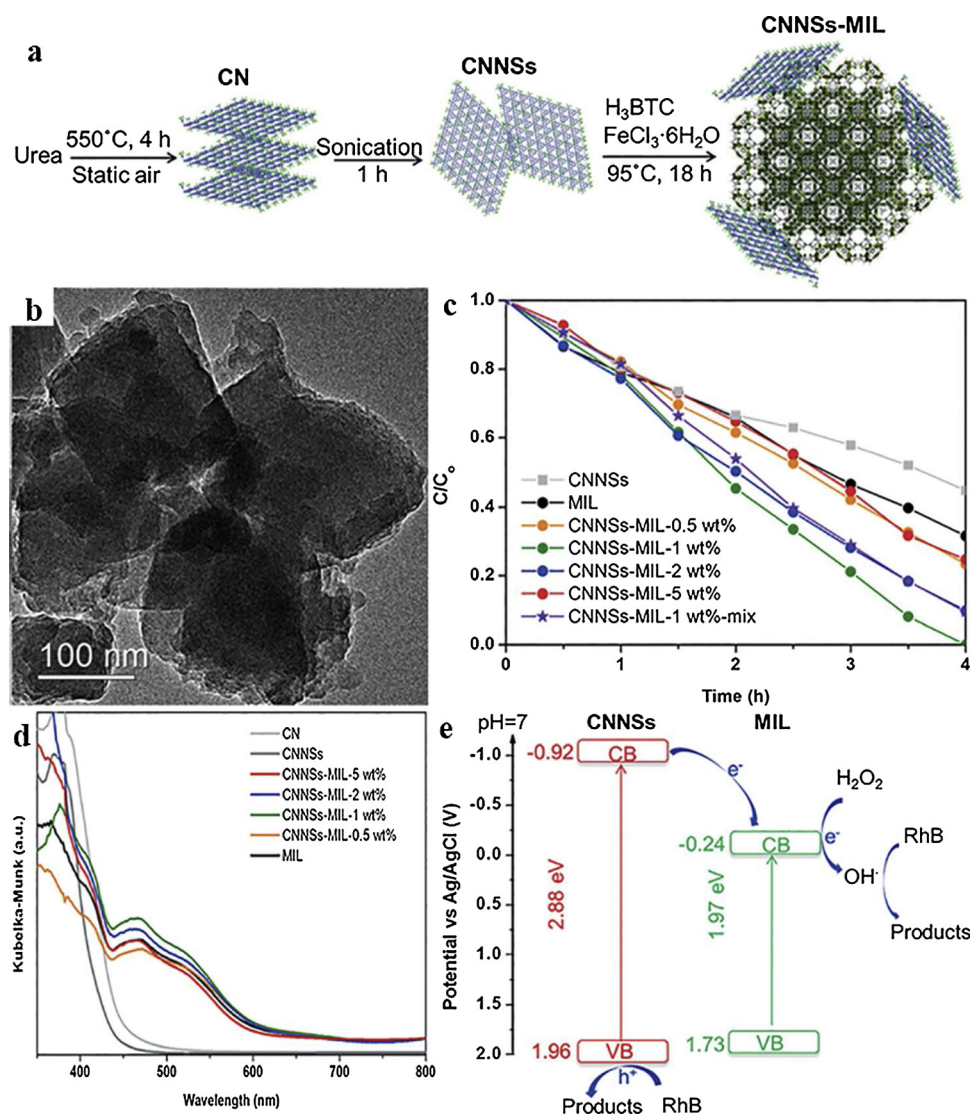
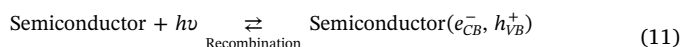


Fig. 13. (a) Overview of the synthesis procedure of CNNSs-MIL-*x* wt% nanocomposites. 1st step: synthesis of bulk CN via calcination of urea. 2nd step: exfoliation of bulk CN via sonication. 3rd step: synthesis of the MOF in the presence of dispersed CNNSs. Abbreviations: CN: bulk carbon nitride; CNNSs: carbon nitride nanosheets; H_3BTC : benzene-1,3,5-tricarboxylic acid; MIL: MIL-100(Fe). (b) TEM images of CNNSs-MIL-1 wt% nanocomposite; (c) Photocatalytic degradation of RhB over CNNSs, MIL, the nanocomposites of CNNSs and MIL-100(Fe) with varying contents of CNNSs, and the physical mixture of CNNSs and MIL (1 wt% of CNNSs). Conditions: 10 mg catalyst in 50 mL of RhB aqueous solution (50 ppm), 0.01 M H_2O_2 . Light source: 150 W Xe lamp equipped with 400 nm filter; (d) UV-vis DRS spectra of bulk carbon nitride (CN), carbon nitride nanosheets (CNNSs), MIL-100(Fe) and the nanocomposites of CNNSs/MIL-100(Fe) with varying contents of CNNSs; (e) Band structure of the nanocomposites of CNNSs and MIL. Potential inhibition of electron-hole recombination is highlighted. A mechanism for the photocatalytic degradation of Rhodamine B using the nanocomposite is proposed [118], copyright (2016) Royal Society of Chemistry.

urea heated at 550 °C in muffle furnace for 4.0 h. Secondly, CN powder was dispersed in EtOH and then exfoliated using a probe sonicator for 60 min. CN nanosheets (CNNSs) were separated from the resulting suspension via centrifugation at 6000 rpm for 5.0 min, 15,000 rpm for 15 min and dried under 60 °C. Thirdly, the mixture of specific amount of CNNSs, FeCl_3 , benzene-1,3,5-tricarboxylic acid, and deionized water was sealed and heated at 95 °C for 18 h. Finally, series CNNSs-MIL-*X* wt% (*X* wt% is the weight percent of CNNSs in the sample). The PXRD, FTIR, SEM, TEM, BET, TGA, UV-vis DRS and PL were used to affirmed the successful fabrication of CNNSs-MIL-*X* wt%. As illustrated in Fig. 13b, the TEM image displayed that the MIL-100(Fe) particles could be observed obviously, but the CNNSs was difficult to detect due to its minor content in the composites.

Compared with bulk CN, blue shift of ca. 20 nm was observed for the absorption edge of CNNSs (Fig. 13d), which might be contributed to the quantum confinement effect [202,203]. The CNNSs-MIL-*X* wt% nanocomposites displayed nearly identical absorbance patterns to that of MIL-100(Fe), in which CNNSs-MIL-1 wt% exhibited the strongest absorbance from 400 to 600 nm. In order to evaluate the photocatalytic activities of the CNNSs-MIL-*X* wt% nanocomposites, RhB was selected as organic pollutant model. With the aid of H_2O_2 , CNNSs-MIL-1 wt% could achieve 100% photocatalytic removal of RhB, exceeding that of individual MIL-100(Fe), CNNSs, physical mixture of MIL-100(Fe) and CNNSs, and other mass ratio CNNSs-MIL-*X* wt% (Fig. 13c). The

photocatalytic RhB degradation performance decreased with the increase of CNNSs up to 1.0, due to the quick photogenerated hole-electron recombination, poor light harness, and decreasing surface area resulted from the stacked CNNSs. The involved photocatalysis mechanism and reactions were displayed in Fig. 13e and Eqs. (11)–(23), respectively. (i) Upon the irradiation of visible light, electrons (e^-) could be excited from the VB of CNNSs (1.96 V) to their CB (-0.92 V), and holes (h^+) were accumulated in their VB (Eq. (11)). (2) The electrons could be moved from CB (-0.92 V) of CNNSs to the CB (-0.24 V) of MIL-100(Fe), which inhibited the recombination of photogenerated electrons and holes in CNNSs. The close VB energy of CNNSs (1.96 V) and MIL-100(Fe) (1.73 V) led to less h^+ transfer between their VBs. The cumulated h^+ in the VB of CNNSs could directly degrade RhB [204,205] (Eq. (17)). (3) The accumulative electrons in the CB of MIL-100(Fe) could react with the added H_2O_2 to form ·OH (Eq. (12)), which could also decompose the RhB [206] (Eq. (16)). Also, the scavenging of h^+ by H_2O_2 as listed in Eqs. (18), (20) and (22) could enhance the oxidative degradation of RhB [206]. In all, the construction of CNNSs-MIL composite achieved better photocatalytic activity toward RhB degradation resulted from enhanced light absorbance, increased surface area and rapid photogenerated electron-hole separation.



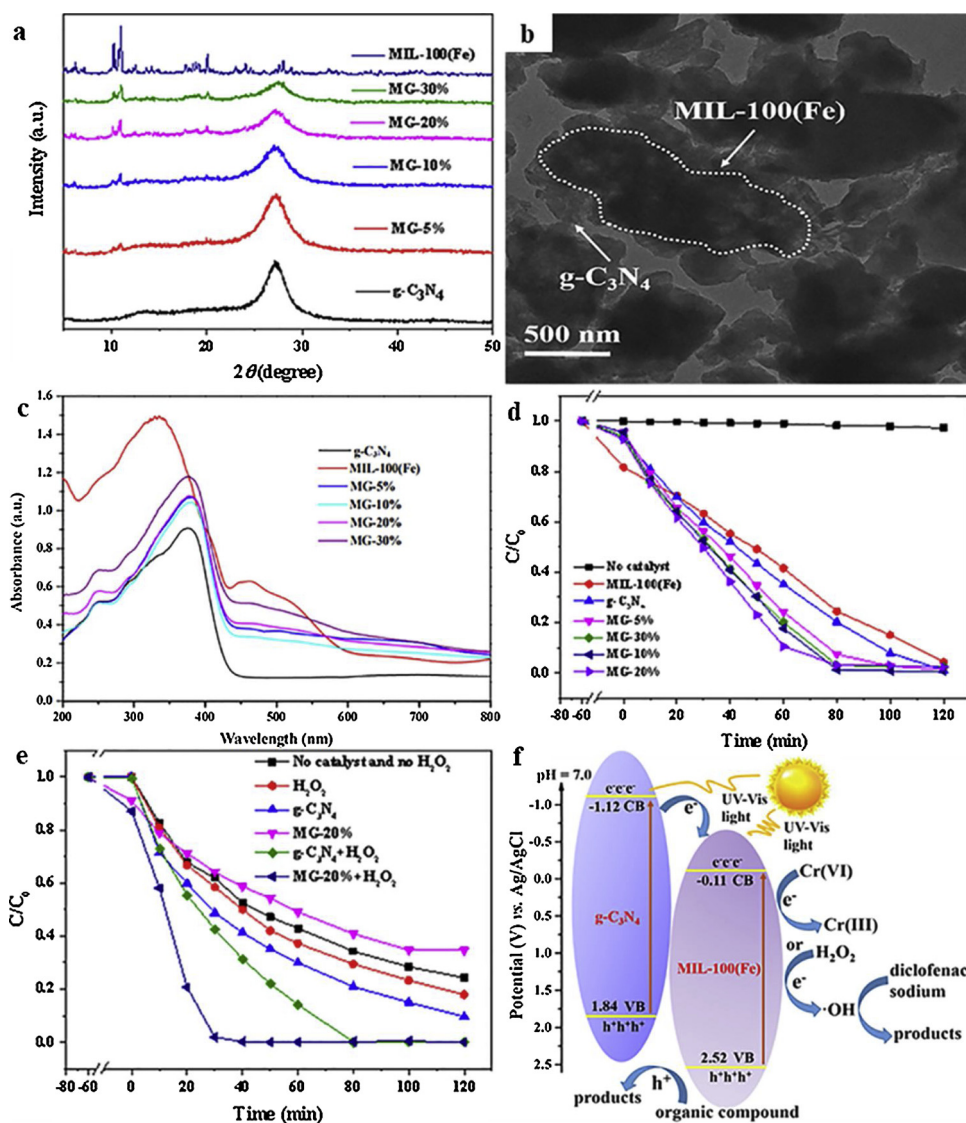


Fig. 14. (a) XRD patterns of g-C₃N₄, MG-*x* (*x* = 5%, 10%, 20%, and 30%) hybrids and MIL-100(Fe); (b) TEM images of MG-20%; (c) UV-vis spectrum of g-C₃N₄, MG-*x* (*x* = 5%, 10%, 20%, and 30%) hybrids and MIL-100(Fe); (d) Cr(VI) reduction photocatalytic performance of MIL-100(Fe), g-C₃N₄ and MG-*x* (*x* = 5%, 10%, 20%, and 30%) hybrids; (e) Photocatalytic degradation of diclofenac sodium under different control conditions; (f) The possible mechanism of photocatalytic reduction of Cr(VI) and degradation of diclofenac sodium over MG-20% [119], copyright (2018) Elsevier.



$$\text{@298K: } E_{\text{H}_2\text{O}_2/\text{HO}^\cdot}(\text{SHE})/\text{V} = 0.9881 - 0.0591\text{pH} + 0.0591\log(\text{H}_2\text{O}_2) - 0.0591\log(\text{HO}^\cdot) \quad (13)$$



$$\text{@298K: } E_{\text{HO}^\cdot/\text{H}_2\text{O}}(\text{SHE})/\text{V} = 2.5384 - 0.0591\text{pH} + 0.0591\log(\text{HO}^\cdot) \quad (15)$$



$$\text{@298K: } E_{\text{HO}_2/\text{H}_2\text{O}_2}(\text{SHE})/\text{V} = 1.4359 - 0.0591\text{pH} + 0.0591\log(\text{HO}_2) - 0.0591\log(\text{H}_2\text{O}_2) \quad (19)$$



$$\text{@298K: } E_{\text{O}_2/\text{HO}_2}(\text{SHE})/\text{V} = -0.0460 - 0.0591\text{pH} - 0.0591\log(\text{HO}_2) + 0.0591\log P_{\text{O}_2} \quad (21)$$



$$\text{@298K: } E_{\text{O}_2/\text{H}_2\text{O}_2}(\text{SHE})/\text{V} = 0.6949 - 0.0591\text{pH} + 0.0296\log P_{\text{O}_2} - 0.0296\log(\text{H}_2\text{O}_2) \quad (23)$$

Wang et al. prepared MIL-100(Fe)/g-C₃N₄ (MG-*x*, *x* is the mass fraction of MIL-100(Fe) in the composite) by ball-milling the mixture of MIL-100(Fe) and g-C₃N₄, followed by thermal treatment at 300 °C for 2 h [119]. The PXRD patterns as illustrated in Fig. 14a confirmed the formation of MIL-100(Fe)/g-C₃N₄ hybrid, in which the characteristic peaks of MIL-100(Fe) (2θ = 6.2, 10.2, 11.0, 20.0°) and g-C₃N₄ (2θ = 27.2°) could be observed. The SEM, TEM and HRTEM images highlighted that the g-C₃N₄ nanosheets were adhered closely onto MIL-100(Fe) (Fig. 14b). The introduction of MIL-100(Fe) into g-C₃N₄ increased the visible light absorbance (Fig. 14c), which enhanced the photocatalytic Cr(VI) reduction performance under visible light irradiation. The increase of MIL-100(Fe) from 0 to 20% in MG-*x* led to

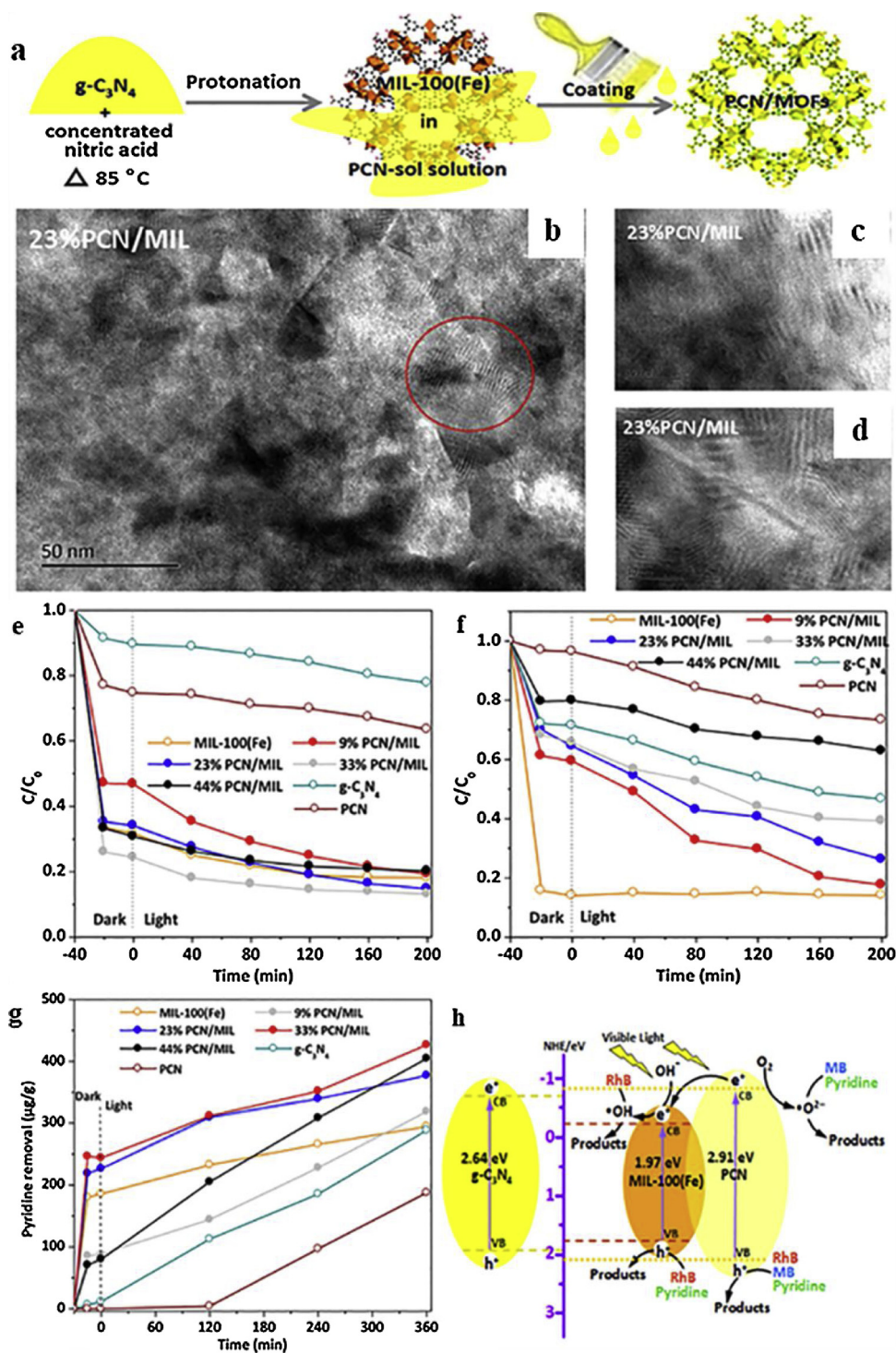


Fig. 15. (a) Illustration of the synthesis of PCN/MIL; (b)–(d) TEM images of 23%PCN/MIL; (e) Photocatalysis profile of RhB degradation over MIL-100(Fe), $g-C_3N_4$, PCN and X%PCN/MIL; (f) Adsorption and photocatalysis profile of MB degradation over MIL-100(Fe), $g-C_3N_4$, PCN and X%PCN/MIL; (g) Photocatalytic oxidation of pyridine by molecular oxygen over MIL-100(Fe), $g-C_3N_4$, PCN and X%PCN/MIL; (h) The schematic illustration of photocatalysis mechanism [117], copyright (2018) Elsevier.

increasing Cr(VI) reduction performance due to both improved visible-light harness and the rapid charge transfer at the heterojunctions (Fig. 14d). Excessive MIL-100(Fe) resulted into declined unfavorable charge transfer at the interface of heterojunctions [107]. Taking MG-20% as example, the photogenerated electrons in the CB of $g-C_3N_4$ (-1.12 V) were transferred to the CB of MIL-100(Fe) (-0.11 V), which facilitated the transformation from Cr(VI) to Cr(III) (Fig. 14f). Under this situation, if the holes produced in the VB of $g-C_3N_4$ (1.84 V) and

MIL-100(Fe) (2.52 V) were consumed by some scavengers like citric acid, oxalic acid and diclofenac sodium, the separation of electrons and holes could be accelerated to achieve efficient Cr(VI) reduction (Fig. 14e).

Considering that both MIL-100(Fe) and $g-C_3N_4$ displayed negative polarity, they are not easily combined together due to the strong and mutual electrostatic repulsion. Song and coworkers developed a facile method (Fig. 15a) to prepared stable protonated $g-C_3N_4$ coated MIL-

Table 3The photocatalytic performances of some ternary MOF/g-C₃N₄/X composites.

Composites	Preparation method	Applications	Ref.
g-C ₃ N ₄ /UiO-66/Ni ₂ P	In-situ deposition of UiO-66 from its precursors on the prepared g-C ₃ N ₄ , followed by in-situ deposition of Ni ₂ P from its precursors on the prepared g-C ₃ N ₄ /UiO-66.	H ₂ production	[209]
BiOI@UiO-66(NH ₂)/g-C ₃ N ₄	In-situ deposition of UiO-66 from its precursors on the prepared g-C ₃ N ₄ , followed by in-situ deposition of BiOI from its precursors on the prepared g-C ₃ N ₄ /UiO-66.	Degradation toward RhB and TC	[210]
Cd _{0.5} Zn _{0.5} S@UiO-66@g-C ₃ N ₄	In-situ deposition of UiO-66 from its precursors on the prepared g-C ₃ N ₄ , followed by in-situ deposition of Cd _{0.5} Zn _{0.5} S from its precursors on the prepared g-C ₃ N ₄ /UiO-66.	H ₂ production and MO degradation.	[211]
CD@UiO-66-NH ₂ /g-C ₃ N ₄	In-situ deposition of UiO-66 from its precursors on the prepared g-C ₃ N ₄ , followed by in-situ deposition of carbon dot from its precursors on the prepared g-C ₃ N ₄ /UiO-66.	H ₂ production	[212]
N-K ₂ Ti ₄ O ₉ /g-C ₃ N ₄ /UiO-66	In-situ deposition of UiO-66 from its precursors on the prepared N-K ₂ Ti ₄ O ₉ /g-C ₃ N ₄ mixture	RhB degradation	[213]
Na _x -C ₃ N ₄ /Pt@UiO-66	In-situ deposition of Pd from its precursors on the prepared UiO-66, followed by in-situ formation of Na _x -C ₃ N ₄ /Pt@UiO-66 via thermal treatment.	H ₂ production	[214]
g-C ₃ N ₄ /ZIF-67/MoS ₂	In-situ deposition of UiO-66 from its precursors on the prepared g-C ₃ N ₄ , followed by in-situ deposition of MoS ₂ from its precursors on the prepared g-C ₃ N ₄ /UiO-66.	H ₂ production	[215]
NH ₂ -MIL-125(Ti)/g-C ₃ N ₄ /NiPd	In-situ deposition of NiPd from its precursors on the prepared NH ₂ -MIL-125(Ti)/g-C ₃ N ₄ mixture	H ₂ production	[216]
MIL-125/Ag/g-C ₃ N ₄	In-situ deposition of Ag from its precursors on the prepared NH ₂ -MIL-125(Ti)/g-C ₃ N ₄ mixture.	Photo-oxidation towards various substituted benzyl alcohols and photo-reduction towards various nitrobenzene derivatives.	[217]
Ni _x -Mo _{1-x} S ₂ /MOF-5@g-C ₃ N ₄	In-situ deposition of MOF-5 from its precursors on the prepared g-C ₃ N ₄ , followed by in-situ deposition of Ni _x -Mo _{1-x} S ₂ from its precursors on the prepared MOF-5@g-C ₃ N ₄ .	H ₂ production	[218]

100(Fe) (PCN/MIL) [117], in which the protonated g-C₃N₄ (PCN) was prepared via stirring the mixture of g-C₃N₄ powder and concentrated HNO₃ under 85 °C for several hours. Taking 23%PCN/MIL as example, its HRTEM images illustrated that the overlapping morphology was formed between MIL-100(Fe) channels and ultrathin PCN sheets (Fig. 15b–d). In this work, the successful PCN coating on MIL-100(Fe) was further confirmed by contact angle measurement. For example, 23%PCN/MIL displayed highly hydrophilic behavior with a contact angle of 0°, which was identical to MIL-100(Fe), while quite different from g-C₃N₄ (135.6°), PCN (26°), mechanically mixed g-C₃N₄ + MIL-100(Fe) (18.9°) and mechanically mixed PCN + MIL-100(Fe) (24.2°). The organic dyes (like RhB and MB) and pyridine were selected to investigate the photocatalytic degradation performance of as-prepared PCN/MIL-100(Fe). The pristine MIL-100(Fe) displayed different adsorption activities toward RhB (1.56 × 1.35 × 0.42 nm) and MB (1.38 × 0.64 × 0.21 nm) [29] due to that the adsorption process was occurred on the outer surface and in the pores of MIL-100(Fe) [207]. As to the removal performance toward RhB, 33%PCN/MIL exhibited highest photocatalytic decomposition (86.9%) with the aid of both adsorption and photocatalysis (Fig. 15e), in which holes were the most active specie to degrade RhB (Fig. 15h). While, 9%PCN/MIL accomplished the optimal photocatalytic activity toward MB resulted from the highly dispersed active species existing over the ultrathin PCN film, in which both superoxide radicals and holes along with hydroxyl radicals are responsible to the MB degradation (Fig. 15f). As to the oxidative denitrogenation of pyridine, 33%PCN/MIL can achieved 400 μg g⁻¹ denitrogenation efficiency within 360 min (Fig. 15g), in which the superoxide radicals and holes played primary roles as highlighted in Fig. 15h. In all, the introduction of protonated g-C₃N₄ could help MIL-100(Fe) regulate its framework structure, surface property along with pore size. As well, the combination of MIL-100(Fe) provided g-C₃N₄ an ideal platform to achieve uniform distribution of active sites, which can help inhibit the electron-hole recombination. Additionally, the higher porosity and surface area felicitated the larger adsorption densities of the targeted pollutants, which could also favor the enhanced photocatalytic performance of PCN/MIL.

3. The current status of g-C₃N₄/MOF/X ternary photocatalysts

Recently, construction of ternary photocatalytic system can be considered as an effective strategy to improve photocatalytic performance because of synergistic effect and well-contacted interfaces in the different components [208]. Considering the merit of MOFs' large surface area, its combination with g-C₃N₄ and/or other semiconductor photocatalysts or noble metal nanoparticles would overcome their disadvantages like low surface area along with the quick electron-hole recombination. Some ternary photocatalytic systems are constructed from MOFs (like UiO-66(-NH₂), ZIF-67, MIL-125 and MOF-5), g-C₃N₄, and semiconductor photocatalysts (like Ni₂P, BiOI, Cd_{0.5}Zn_{0.5}S, carbon nanodots, N-K₂Ti₄O₉, MoS₂ and NiPd) or noble metal nanoparticles (like Pt and Ag), as listed in Table 3. In this review, UiO-66/g-C₃N₄/X (X = semiconductor photocatalysts or noble metal nanoparticles) ternary composites were selected as representatives to highlight their fabrication methods, characterizations, photocatalytic performances and corresponding mechanism.

3.1. g-C₃N₄/UiO-66/Ni₂P

The hexagonal nickel phosphide (Ni₂P) can act as outstanding hydrogen generation catalyst under acidic, neutral and basic conditions [219,220]. The combination of Ni₂P with semiconductors like ZnS, CdS, Cd_{0.5}Zn_{0.5}S can enhance the hydrogen evolution activities [219–221]. UiO-66 and g-C₃N₄ were introduced to further increase Ni₂P's photocatalytic performance via increasing the specific surface area and active sites [209]. The formation of Ni₂P onto UiO-66 possessed minor effect on its morphology (Fig. 16a), which was confirmed by SEM, TEM, XRD, FTIR and XPS. Compared with g-C₃N₄/Ni₂P and g-C₃N₄/UiO-66, the construction of g-C₃N₄/UiO-66/Ni₂P enhanced the light absorption intensity from 450 nm to 800 nm (Fig. 16b). As well, the formation of g-C₃N₄/UiO-66/Ni₂P accomplished narrower bandgap (2.85 eV) than that of g-C₃N₄/Ni₂P (50%) (2.98 eV) and g-C₃N₄/UiO-66 (2.99 eV), as illustrated in Fig. 16c. The narrower band gap induced easier electrons transition from VB to CB [222,223]. The optimal proportion of g-C₃N₄/UiO-66/Ni₂P (50%) achieved best catalytic activity to produce H₂ under visible light (λ > 420 nm) due to the quick separation of

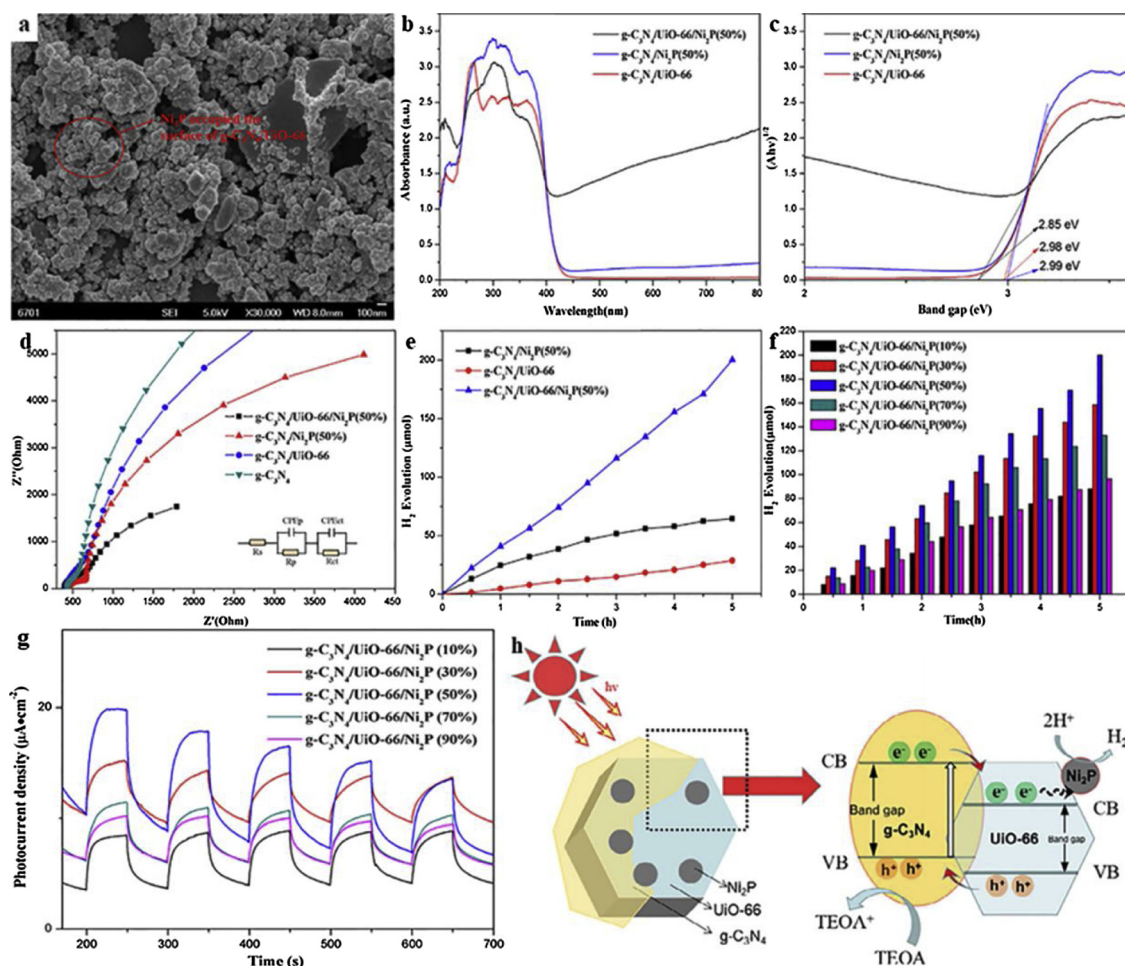


Fig. 16. (a) SEM images of the as-obtained $g\text{-C}_3\text{N}_4/\text{UiO-66}/\text{Ni}_2\text{P}$ (50%); (b) The UV–vis absorption spectra and (c) the forbidden band width of $g\text{-C}_3\text{N}_4/\text{Ni}_2\text{P}$ (50%), $g\text{-C}_3\text{N}_4/\text{UiO-66}$ and $g\text{-C}_3\text{N}_4/\text{UiO-66}/\text{Ni}_2\text{P}$ (50%); (d) The EIS pattern of as-prepared samples; (e) Hydrogen production trend of different component photocatalysts; (f) Hydrogen production of photocatalysts with different contents of Ni_2P ; (g) Photocurrent response of photocatalysts with different contents of Ni_2P under visible light irradiation ($\lambda > 420 \text{ nm}$); (h) The schematic illustration of the possible mechanism [209], copyright (2018) Elsevier.

electron-hole pairs and more active reaction sites, which was superior to $g\text{-C}_3\text{N}_4$, $g\text{-C}_3\text{N}_4/\text{Ni}_2\text{P}$ and $g\text{-C}_3\text{N}_4/\text{UiO-66}$, respectively (Fig. 16d–f). The electrochemical determination (photocurrent response, electrochemical impedance spectroscopy (EIS), LSV curves) and photoluminescence (PL) spectra could clarified the enhanced photocatalytic performance (16 g). As depicted in Fig. 16h, upon the visible light illumination, the electrons were excited to escape from $g\text{-C}_3\text{N}_4$ to UiO-66, which inhibited the recombination of electron-hole. While, the accumulated electrons over the Ni_2P were responsible to the H_2 production. This work concerning the construction of $g\text{-C}_3\text{N}_4/\text{UiO-66}/\text{Ni}_2\text{P}$ demonstrated how the ternary composite photocatalyst can enhance the photocatalytic performances.

3.2. $g\text{-C}_3\text{N}_4/\text{UiO-66}/\text{BiOI}$

As a p-type semiconductor, BiOI exhibited excellent photocatalytic performance upon the visible light irradiation due to its narrow band gap (1.7–1.8 eV) and anisotropic layered structure [224]. Considering that the photocatalytic performance of pure BiOI was restricted by its quick recombination of photoinduced electron-hole and poor conductivity [225–227], some photocatalysts like metal oxides (ZnO) [228], $g\text{-C}_3\text{N}_4$ [229,230], graphene [231], MOFs (MIL-88) [232] were introduced to improve the photocatalytic activity of BiOI. To further overcome the disadvantages of BiOI and/or C_3N_4 like low surface area and fast recombination of charge carries, MOFs were selected to construct composites, as they can provide more channels to transfer the

photoinduced electrons and achieve quick electron-hole separation. Li and coworkers adopted BiOI, $g\text{-C}_3\text{N}_4$ and UiO-66- NH_2 to construct ternary composites via in situ solvothermal and hydrothermal methods (as shown in Fig. 17a) to accomplish increasing surface area, enhancing visible light response and fast electron-hole separation with the aid of internal electric field in the heterojunction interface [210]. The successful fabrication of ternary composites $\text{BiOI}@\text{UiO-66}(\text{NH}_2)@g\text{-C}_3\text{N}_4$ ($\text{BiOI}@\text{UNCN}$) was confirmed by SEM (Fig. 17b), TEM (Fig. 17c), PXRD, FTIR, BET and XPS. Series $\text{BiOI}@\text{UNCN}$ composites were used to conduct photocatalytic degradation toward RhB and TC with initial concentration of 20 mg/L. As illustrated in Fig. 17d and e, $\text{BiOI}@\text{UNCN-40}$ exhibited best photocatalytic degradation efficiencies toward RhB (95%) and TC (80%), which were better than those of individual BiOI, UiO-66- NH_2 , $\text{UiO-66}(\text{NH}_2)@g\text{-C}_3\text{N}_4$, respectively. The electrochemical impedance spectra revealed that the $\text{BiOI}@\text{UNCN-40}$ displayed smaller arc radius of the semicircular Nyquist plot than that of BiOI and UiO-66- NH_2 , implying $\text{BiOI}@\text{UNCN-40}$ heterojunction possessed smallest electron transfer resistance and best charge transfer efficiency [233]. As shown in Fig. 17g, upon the visible light illumination, all BiOI, UiO-66- NH_2 and $g\text{-C}_3\text{N}_4$ are excited to produce photogenerated electron-hole, in which the electrons in CB of BiOI can be captured by the holes formed in the CB of UiO-66- NH_2 and $g\text{-C}_3\text{N}_4$, while the leaving holes can degrade RhB and TC directly. The CB of $g\text{-C}_3\text{N}_4$ (−1.08 eV vs NHE) and UiO-66- NH_2 (−0.51 eV vs NHE) is more negative than that of $\text{O}_2/\cdot\text{O}_2^-$ (−0.33 eV vs NHE). While, the corresponding photoexcited electrons in their CBs can combine with O_2 to form $\cdot\text{O}_2^-$, which are responsible to decompose

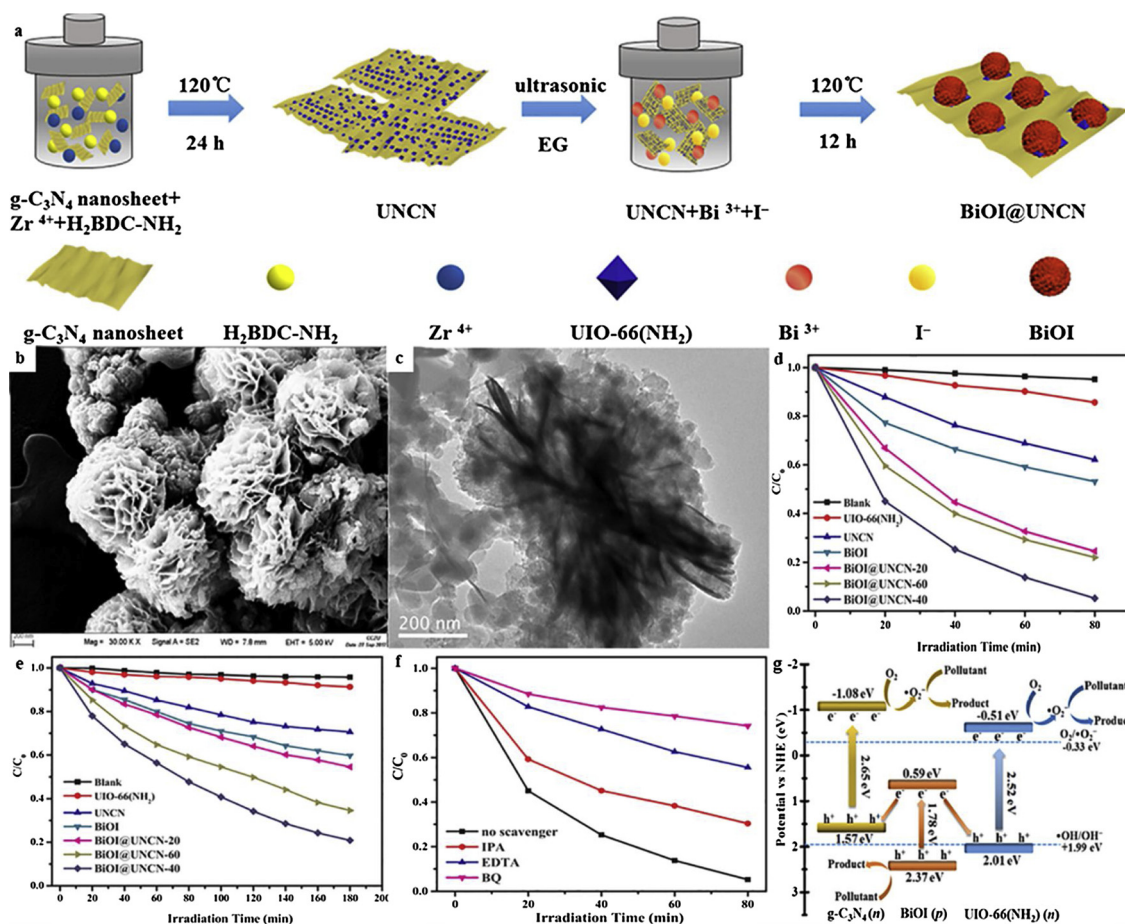


Fig. 17. (a) Schematic illustration for the preparation of BiOI@UNCN heterojunction; (b) SEM image of BiOI@UNCN (inset); Photocatalytic degradation of (d) RhB and (e) TC over the as-prepared samples under visible-light irradiation ($\lambda \geq 420$ nm); (f) Effects of different scavengers on the degradation of RhB on BiOI@UNCN-40; (g) Schematic illustration of photocatalytic degradation over the BiOI@UNCN-40 under visible light irradiation [210], copyright (2018) Elsevier.

RhB and TC. As well, the accumulative holes on the VB of BiOI can oxidize OH^- to form $\cdot\text{OH}$ radicals. The active species trapping experiments with the addition of IPA, EDTA and BQ revealed that $\cdot\text{O}_2^-$ was the primary active specie along with h^+ and $\cdot\text{OH}$ were the secondary active species in the photocatalytic reaction over BiOI@UNCN-40 (Fig. 17f). It was concluded that the superior photocatalytic activity and chemical stability of BiOI@UNCN-40 could be attributed to the construction of n-p-n junction intrinsic electric field in the ternary, which can enhance charge carrier separation driven by Z-scheme mechanism, and high surface area subject to UiO-66-NH₂. The sample of BiOI@UiO-66(NH₂)@ $\text{g-C}_3\text{N}_4$ composite provided a useful approach to design a new Z-scheme ternary photocatalytic system toward organic pollutants degradation.

3.3. $\text{g-C}_3\text{N}_4/\text{UiO-66}/\text{Cd}_{0.5}\text{Zn}_{0.5}\text{S}$

Metal sulfides like CdS as photocatalysts attracted increasing attentions due to their appropriate band gap and outstanding photoelectric properties [234], in which the binary metal sulfides like $\text{Cd}_{1-x}\text{Zn}_x\text{S}$ displayed better photocatalytic performance [235,236]. Just similar to CdS, $\text{Cd}_{1-x}\text{Zn}_x\text{S}$ suffered from serious photocorrosion and carrier charge recombination. To overcome the above-stated disadvantages, the heterojunction composites like $\text{Cd}_{0.5}\text{Zn}_{0.5}\text{S}/\text{g-C}_3\text{N}_4$ [237], $\text{Zn}_{0.5}\text{Cd}_{0.5}\text{S}/\text{RGO}$ [238], $\text{Cd}_{0.5}\text{Zn}_{0.5}\text{S}/\text{ZIF-8}$ [140], $\text{Cd}_{0.5}\text{Zn}_{0.5}\text{S}/\text{g-C}_3\text{N}_4$ [239] and $\text{Cd}_{0.2}\text{Zn}_{0.8}\text{S}/\text{UiO-66-NH}_2$ [240] were fabricated to modify the activity of $\text{Cd}_{1-x}\text{Zn}_x\text{S}$. Recently, MOFs with high surface area were introduced to construct ternary photocatalytic systems to further

improve the photocatalytic performance of $\text{Cd}_{1-x}\text{Zn}_x\text{S}$. Li and coworkers developed an in-situ hydrothermal reaction and precipitation strategy as shown in Fig. 18a to construct a novel ternary composite $\text{Cd}_{0.5}\text{Zn}_{0.5}\text{S}/\text{UiO-66}/\text{g-C}_3\text{N}_4$, which displayed better photocatalytic performances toward H_2 evolution (Fig. 17e) and MO decomposition (Fig. 17f) under the illumination of visible light than those of $\text{Cd}_{0.5}\text{Zn}_{0.5}\text{S}$, $\text{UiO-66}/\text{g-C}_3\text{N}_4$, $\text{CdS}/\text{UiO-66}/\text{g-C}_3\text{N}_4$ and $\text{ZnS}/\text{UiO-66}/\text{g-C}_3\text{N}_4$, respectively [211]. The enhanced photocatalytic activities were confirmed by photoluminescence (PL) spectra, UV-vis DRS spectra and energy band determination (Fig. 18b–d). The active species capture experiment results revealed that $\cdot\text{O}_2^-$ and h^+ are the major active species to decompose MO, and $\cdot\text{OH}$ radicals only played minor role in the photocatalytic process. As illustrated in Fig. 18g and h, upon the irradiation of visible light, $\text{Cd}_{0.5}\text{Zn}_{0.5}\text{S}$ and $\text{g-C}_3\text{N}_4$ could be excited to produce photo-induced electron-hole pairs. On the contrary, UiO-66 couldn't be excited by visible light due to its large band gap. The excited electrons on the CB of $\text{g-C}_3\text{N}_4$ (-1.21 eV vs NHE) could be transferred to that of $\text{Cd}_{0.5}\text{Zn}_{0.5}\text{S}$ (-0.56 eV vs NHE) [241], and then moved to the LUMO of UiO-66, which led to fast separation of photogenerated electron-hole pairs (Fig. 18g). The H_2 evolution was achieved as the excited electrons were effectively transferred to H^+ (Fig. 18h), which was ascribed to that the LUMO of UiO-66 (-0.18 eV vs NHE) [242] is more negative than the redox potential of H^+/H_2 [243]. And the organic pollutant MO was degraded by the $\cdot\text{O}_2^-$ formed from the reaction between e^- on the LUMO of UiO-66 and adsorbed O_2 along with the h^+ accumulated on the VB of $\text{g-C}_3\text{N}_4$, being affirmed by the results of active species trapping experiments. The enhanced photocatalytic activity of

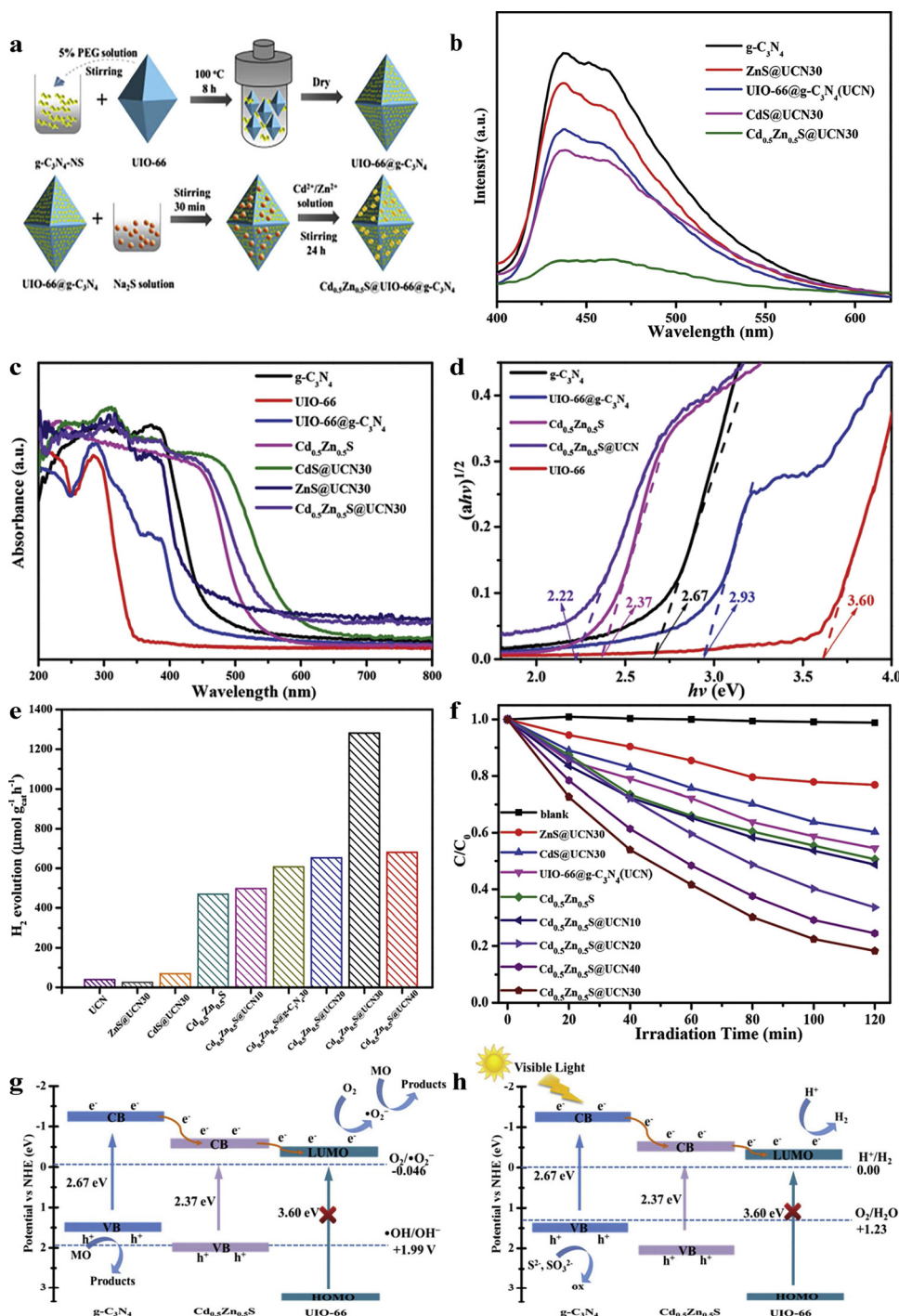


Fig. 18. (a) Schematic illustration for the preparation of the $\text{Cd}_{0.5}\text{Zn}_{0.5}\text{S}@ \text{UiO-66}@ \text{g-C}_3\text{N}_4$ heterojunction; (b) Photoluminescence spectra of $\text{g-C}_3\text{N}_4$, $\text{UiO-66}@ \text{g-C}_3\text{N}_4$, $\text{ZnS}@ \text{UCN30}$, $\text{CdS}@ \text{UCN30}$ and $\text{Cd}_{0.5}\text{Zn}_{0.5}\text{S}@ \text{UCN30}$; (c) UV-vis DRS spectra and (d) plots of the $(\alpha h\nu)^{1/2}$ versus photo energy ($h\nu$) for $\text{g-C}_3\text{N}_4$, UiO-66 , $\text{UiO-66}@ \text{g-C}_3\text{N}_4$, $\text{Cd}_{0.5}\text{Zn}_{0.5}\text{S}$ and $\text{Cd}_{0.5}\text{Zn}_{0.5}\text{S}@ \text{UCN30}$; (e) Photocatalytic H_2 evolution rate under visible light irradiation over the as-prepared samples (Na_2S and Na_2SO_3 were used as the hole-scavenger without noble metal co-catalysts); (f) Photocatalytic degradation of MO over the as-prepared samples under visible-light irradiation ($\lambda \geq 420$ nm); (g) Schematic of photocatalytic hydrogen evolution and (h) degradation over the $\text{Cd}_{0.5}\text{Zn}_{0.5}\text{S}@ \text{UCN}$ under visible light irradiation [211], copyright (2018) Royal Society of Chemistry.

$\text{Cd}_{0.5}\text{Zn}_{0.5}\text{S}@ \text{UiO-66}@ \text{g-C}_3\text{N}_4$ could be ascribed to its large surface area originated from UiO-66 , improved visible light absorption range along with fast separation of carrier charges. The last one could be further affirmed by the results of photocurrent and EIS determinations. The successful construction of $\text{Cd}_{0.5}\text{Zn}_{0.5}\text{S}@ \text{UiO-66}@ \text{g-C}_3\text{N}_4$ with outstanding photocatalytic performance provided a new insight into the fabrication of advanced ternary noble-metal-free heterojunctions toward highly-efficient photocatalytic applications in the field of energy production and pollution elimination.

3.4. $\text{g-C}_3\text{N}_4/\text{UiO-66}/\text{CD}$

Carbon nanodots (CDs) have generated enormous excitement in

photocatalytic area due to their efficient light harvesting and outstanding photo-induced electron transfer ability [244–246]. Interfacing CDs with $\text{g-C}_3\text{N}_4$ produces a metal-free system which has recently exhibited significant enhancement of photocatalytic activities for water splitting into hydrogen [247–251], CO_2 reduction [248,252], organic pollutants degradation [253,254]. Zhang and coworkers introduced carbon nanodots (CDs) into $\text{UiO-66-NH}_2/\text{g-C}_3\text{N}_4$ to construct ternary $\text{CD}@ \text{UiO-66-NH}_2/\text{g-C}_3\text{N}_4$ composite photocatalyst (Fig. 19a) to enhance the photocatalytic H_2 production under visible light illumination [212]. The successful fabrication of these ternary composites were characterized by series techniques including but not limited to SEM (Fig. 19b) and TEM (Fig. 19c). The color of as-prepared $\text{CD}@ \text{UiO-66-NH}_2/\text{g-C}_3\text{N}_4$ is brown yellow, and its absorption edge exhibited a

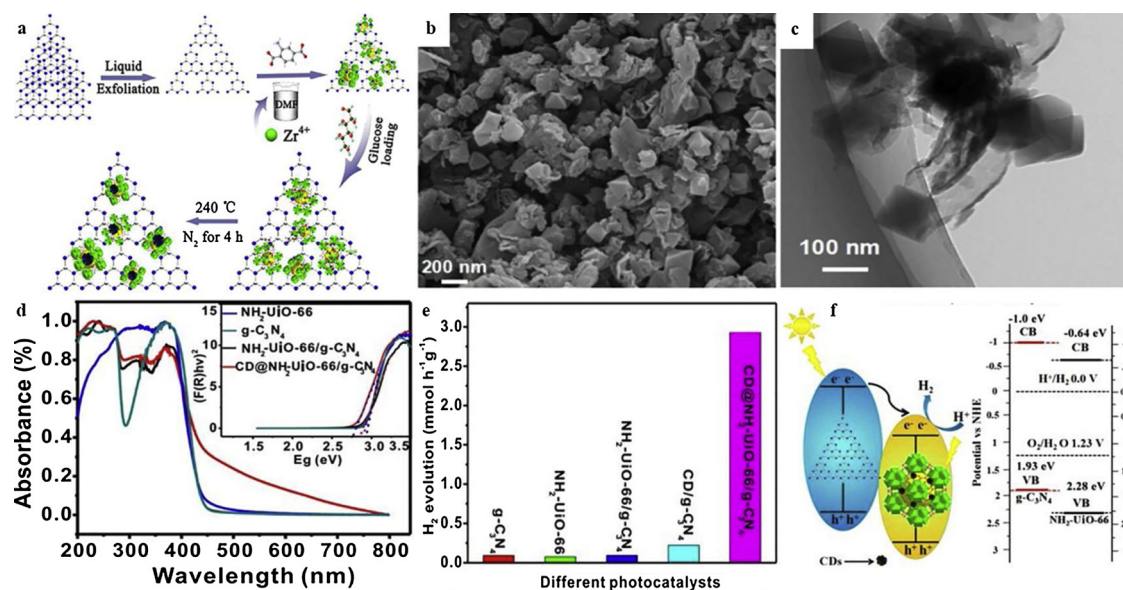


Fig. 19. (a) Schematic illustration for the synthesis of CD@NH₂-Uio-66/g-C₃N₄; (b) SEM image of CD@NH₂-Uio-66/g-C₃N₄; (c) TEM images of CD@NH₂-Uio-66/g-C₃N₄; (d) DRS spectra and tauc plots of g-C₃N₄, NH₂-Uio-66, NH₂-Uio-66/g-C₃N₄ and CD@NH₂-Uio-66/g-C₃N₄ (inset); (e) Photocatalytic H₂ generation rates for g-C₃N₄, NH₂-Uio-66, NH₂-Uio-66/g-C₃N₄, CD/g-C₃N₄ and CD@NH₂-Uio-66/g-C₃N₄ under visible light ($\lambda > 420$ nm); (f) The proposed mechanism for the photocatalytic process of CD@NH₂-Uio-66/g-C₃N₄ [212], copyright (2018) American Chemical Society.

substantial shift up to 800 nm (Fig. 19d). The photocatalytic activities of the CD@Uio-66-NH₂/g-C₃N₄ composites were validated via H₂ production from water splitting upon the irradiation of visible light adopting sodium ascorbate as sacrificial agent. The optimum CD@Uio-66-NH₂/g-C₃N₄ composite with CD content of 2.77 wt% can accomplish the H₂ production rate of 2.930 mmol h⁻¹ g⁻¹ upon the visible light irradiation, which was 32.4, 38.6 and 17.5 times higher than that of individual g-C₃N₄, Uio-66-NH₂ and Uio-66-NH₂/g-C₃N₄, respectively (Fig. 19e). The g-C₃N₄ possessed similar light absorption with Uio-66-NH₂, but the CB of g-C₃N₄ (-1.0 eV vs NHE) is more negative than that of Uio-66-NH₂ (-0.64 eV vs NHE), implying that more photoinduced electron on the CB of g-C₃N₄ could move to the CB of Uio-66-NH₂ (Fig. 19f). The embedded CDs as effective cocatalyst could export the electrons on the CB of Uio-66-NH₂ to reduce H⁺ into H₂. The added sodium ascorbate can consume the accumulated holes on the VB of g-C₃N₄ and Uio-66-NH₂ to increase the H₂ production rate. As well, the introduction of CDs into Uio-66-NH₂/g-C₃N₄ increased the visible light harvesting ability, which facilitated the H₂ production. In conclusion, the CDs in the ternary composite acted as electron transfer station to achieve quick charge separation, enhanced light absorption and long lifetime of photo-induced carriers. This work implied that encapsulating CDs into the pores of MOFs-based composite is an effective strategy to accomplish enhanced photocatalytic performance.

3.5. Na_x-C₃N₄/Pt@Uio-66

The Density-Functional Theory (DFT) calculations revealed that alkali metals (like K or Na) doping can narrow the bandgap of g-C₃N₄ [255,256]. In detail, K atoms can bridge the layers to achieve the decrease of the electronic localization and even extension of the π conjugated system, while Na atoms tended to be doped into the C₃N₄ planes, which increased its in-planar electron density [257,258]. Jiang and coworkers developed Na_x-C₃N₄/Pt@Uio-66 heterojunction composites (x is the molar concentration of Na precursor solution) [214], in which the optimal Na_{0.02}-C₃N₄/Pt@Uio-66 accomplished a good balance between visible-light harvest and electron transfer efficiency to arise enhanced photocatalytic hydrogen production (Fig. 20a). As demonstrated in Fig. 20b and c, the TEM and SEM results revealed that the close contact was formed between Na_x-C₃N₄ and Pt@Uio-66

resulted from their π - π stacking, which was further affirmed by XPS results. The optimized Na content in Na_x-C₃N₄/Pt@Uio-66 led to improved visible-light harvesting capacity (Fig. 20d) and subsequent enhanced H₂ production activity (Fig. 20e), confirmed by the electron paramagnetic resonance (EPR), photoluminescence (PL) spectroscopy, photocurrent response and electrochemical impedance spectroscopy. Two factors like electron transfer and the Na content heavily influenced the Na_x-C₃N₄/Pt@Uio-66 composites' photocatalytic activities [259]. In detail, electron trap site by Na doping is major influence factor as the Na content was less than 0.02 M, while the energy level difference played a major role in the electron transfer process when the Na content was higher than 0.02 M. In all, the Na_x-C₃N₄/Pt@Uio-66 composites with characteristics like regulatable light-harvesting abilities and tunable band structures were prepared, in which both the light-harvesting ability and the electron transfer originated from electron trap sites and energy level difference illustrated saddle-shaped curve with the increase of Na loading. The optimal Na_{0.02}-C₃N₄/Pt@Uio-66 presented the highest H₂ production rate among all other counterparts (Fig. 20e). This innovative work offered an ideal strategy to construct the g-C₃N₄/MOF heterojunctions for enhanced photocatalysis.

4. Conclusions and outlook

Up to now, two synthesis strategies are adopted to prepared g-C₃N₄/MOF binary composites: (i) physical mixing like electrostatic self-assembly, ball-milling or/and thermal annealing treatments toward the g-C₃N₄ and MOF matrix; (ii) in-situ formation of MOF from its precursors on the prepared g-C₃N₄. The former is mixing the two components at macroscale, while the latter is nanoscale mixing, which can provide improved carrier charge transfer. As to g-C₃N₄/MOF/semiconductor ternary composites, the general fabrication strategy adopted is in-situ deposition of MOF from its precursors on the prepared g-C₃N₄ followed by in-situ deposition of semiconductor from its precursors on the prepared g-C₃N₄/MOF. In most case, MOFs offer excellent supports for g-C₃N₄ (or even the third nanocomponent) in highly dispersed and active state, which enlarge the surface area of composites. As well, some researchers tuned the g-C₃N₄ into nanorods, nanotubes, nanosheets, on which some MOFs like ZIF-8, Uio-66, MIL-100 and MIL-125 in nanoparticle state were deposited. The coupling MOFs with g-C₃N₄ (perhaps

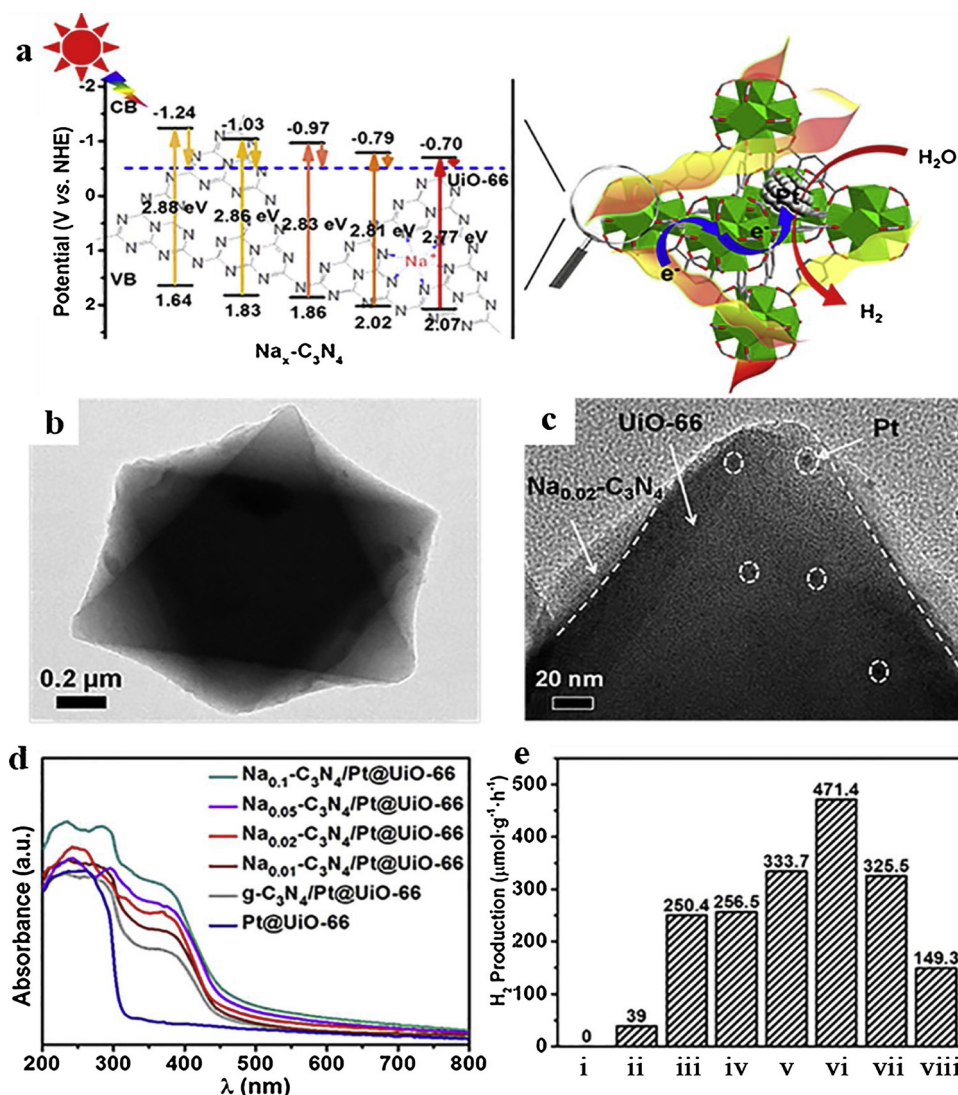


Fig. 20. (a) Schematic illustration showing the photocatalytic hydrogen production over $\text{Na}_x\text{-C}_3\text{N}_4/\text{Pt@UiO-66}$ heterojunction composites, highlighting the tunable band structures; (b) TEM image of $\text{Na}_{0.02}\text{-C}_3\text{N}_4/\text{Pt@UiO-66}$; (c) Enlarged TEM image of $\text{Na}_{0.02}\text{-C}_3\text{N}_4/\text{Pt@UiO-66}$; (d) UV-vis absorption spectra of $\text{Na}_x\text{-C}_3\text{N}_4/\text{Pt@UiO-66}$ and Pt@UiO-66 and (e) the photocatalytic hydrogen production of UiO-66 (i), $\text{Na}_{0.02}\text{-C}_3\text{N}_4$ (ii), physical mixture of $\text{Na}_{0.02}\text{-C}_3\text{N}_4/\text{Pt@UiO-66}$ (iii) and $\text{Na}_x\text{-C}_3\text{N}_4/\text{Pt@UiO-66}$ ($x = 0, 0.01, 0.02, 0.05$, and 0.1 M corresponding to iv-viii) in $\text{MeCN}/\text{TEA}/\text{H}_2\text{O}$ (29.5 : 0.5 : 0.15 v/v, 30 mL) [214], Copyright (2018) Wiley.

the third component can also be introduced) can facilitate the photo-generated carrier charge separation and broaden the light (especially visible light) response range, finally leading to better photocatalytic activities of $\text{g-C}_3\text{N}_4/\text{MOFs}$ than that of their physical mixture. In detail, the prepared heterojunction composites between $\text{g-C}_3\text{N}_4$ and MOFs accomplished some merits: (i) the (visible) light harvesting ability was enhanced; (ii) the carrier charge transfer across the interface was accelerated, and the charge transfer distance was shortened, which heavily inhibited the photoinduced carrier charge recombination.

Despite the significant advances in the $\text{C}_3\text{N}_4/\text{MOF}$ heterostructure composites as photocatalysts, there are still some issues to be considered in the future research work. The morphology and composition of $\text{g-C}_3\text{N}_4$ should be further tuned. More efficient strategies should be applied for the modification of $\text{g-C}_3\text{N}_4$ [67,74,76]: (i) the bulky $\text{g-C}_3\text{N}_4$ can be exfoliated into monolayer or thin-layer nanosheet, which can achieve higher surface area, shorter transfer distance of photoinduced carriers, and quicker diffusion of reactants/products [260–263]; (ii) Element doping can be adopted to achieve structure defect, which is a major method to modify the electronic structure of C_3N_4 [260,263–272]; (iii) The surface can be further modified like the introduction of amine [270,273] and hydroxyl group [274] and so on to

enhance the surface adsorption of reactants and inhibit the recombination of photoinduced electrons-holes pairs [275]; (iv) The crystal structure can be further modulated into amorphous to optimize the band structure, which can accomplish wider light absorption range due to its narrowed band gap [276]; (v) The morphology can be tuned into nanostructures like mesoporous [277,278], nanotube [279,280], hollow nanosphere [281,282], nanorods [283,284] to achieve abundant pores, larger surface area, multiple light-scattering effect and improved mass diffusion of reactants/final products. On the other hand, some efforts should be devoted to get cheap, water/light/thermal/chemical stable, efficient MOF photocatalysts. (i) Kilogram level high-throughput preparation techniques should be adopted, which include but not limited to microwave-assisted synthesis, sonochemical synthesis, electrochemical synthesis and mechanochemical synthesis [19,28,29,31,285]. (ii) It is expected to prepare nanoscale MOFs [286–288], even in monolayer [289] form with abundant coordinately unsaturated metal sites, which can improve the MOFs photocatalytic performances. (iii) The morphology control of MOFs regulated by solvents or surfactants like polyvinylpyrrolidone (PVP) and cetyltrimethylammonium bromide (CTAB) should be paid more attentions [20,22,290,291]. (iv) Gascon and co-workers once pointed out that

semiconducting behavior (CB-VB) only occurs in a very limited subset of MOFs, and HOMO-LUMO gap terminology should be utilized to describe the photocatalytic behaviors in the most MOFs as molecular catalysts [29,292,293]. In the future work, more efforts should be put to identify whether some specific MOFs should be labeled as semiconductor or molecular photocatalysts.

As to the application of g-C₃N₄/MOF composites, further works should be conducted in future. (i) Some theoretical calculations like density functional theory (DFT) were adopted to affirm the structure-property relationship; (ii) The influence factors affecting the photocatalytic activities should be investigated. When g-C₃N₄/MOF composites were used to conduct water environment remediation, the factors like pollutant concentration, co-existing ions (salinity) and dissolved organic matters (DOM) should be considered. Also, the photocatalytic removal performances g-C₃N₄/MOF composites toward pollutants (like Cr(VI) and organic pollutants) in real wastewater under real sunlight irradiation should be evaluated. Especially, more organic pollutants models like Pharmaceutical and Personal Care Products (PPCPs) and perfluorinated organic compounds (PFCs) should be selected to test the g-C₃N₄/MOF composites' photocatalytic degradation efficiencies, in which the TOC removal percentage (degree of materialization) not only maximum absorbance of specific organic pollutant was suggested to determined. Up to now, few reported cases dealt with the pathway of organic decomposition with g-C₃N₄/MOF composites as photocatalysts. In the future, mass spectra are suggested to determine the intermediate products and final products to clarify the degradation pathway.

Considering that both pristine g-C₃N₄ and MOFs are star photocatalysts in the field of H₂ evolution via water splitting, CO₂ reduction, Cr(VI) reduction and organic pollutants degradation, their composites will achieve enhanced photocatalytic performances via combining of their merits and overcoming their disadvantages. It was expected that the current synthesis methods, photocatalytic performances, mechanism and even challenges for g-C₃N₄/MOFs composites highlighted in this review can provide new insight in the exploration and utilization of these composites. In all, we believe that the present studies provide stimuli to carry out intensive research in g-C₃N₄/MOFs composite photocatalysts, and open a new perspective for the sustainable development with the aid of these emerging photocatalytic systems.

Acknowledgements

This work was supported by the National Natural Science Foundation of China (51578034, 51878023), Great Wall Scholars Training Program Project of Beijing Municipality Universities (CIT&TCD20180323), the Project of Construction of Innovation Teams and Teacher Career Development for Universities and Colleges under Beijing Municipality (IDHT20170508), the Beijing Talent Project (2018A35), and Beijing Advanced Innovation Center for Future Urban Design (No. UDC2016030200).

References

- [1] L. Jeongyong, O.K. Farha, R. John, K.A. Scheidt, S.B.T. Nguyen, J.T. Hupp, *Chem. Soc. Rev.* 38 (2009) 1450–1459.
- [2] P. García-García, M. Müller, A. Corma, *Chem. Sci.* 5 (2014) 2979–3007.
- [3] C.J. Doonan, C.J. Sumby, *CrystEngComm* 19 (2017) 4044–4048.
- [4] O.K. Farha, A.Ö. Yazaydin, I. Eryazici, C.D. Malliakas, B.G. Hauser, M.G. Kanatzidis, S.T. Nguyen, R.Q. Snurr, J.T. Hupp, *Nat. Chem.* 2 (2010) 944–948.
- [5] H.-C.J. Zhou, S. Kitagawa, *Chem. Soc. Rev.* 43 (2014) 5415–5418.
- [6] H. Lan, L. Li, X. An, F. Liu, C. Chen, H. Liu, J. Qu, *Appl. Catal. B: Environ.* 204 (2017) 49–57.
- [7] J.-R. Li, R.J. Kuppler, H.-C. Zhou, *Chem. Soc. Rev.* 38 (2009) 1477–1504.
- [8] T. Rodenas, I. Luz, G. Prieto, B. Seoane, H. Miro, A. Corma, F. Kapteijn, F.X. Llabrés i Xamena, J. Gascon, *Nat. Mater.* 14 (2014) 48–55.
- [9] W. Huang, N. Liu, X. Zhang, M. Wu, L. Tang, *Appl. Surf. Sci.* 425 (2017) 107–116.
- [10] X.-Y. Xu, C. Chu, H. Fu, X.-D. Du, P. Wang, W. Zheng, C.-C. Wang, *Chem. Eng. J.* 350 (2018) 436–444.
- [11] A. Liu, C.-C. Wang, C.-z. Wang, H.-f. Fu, W. Peng, Y.-L. Cao, H.-Y. Chu, A.-F. Du, J. Colloid Interface Sci. 512 (2018) 730–739.

- [12] X.-D. Du, C.-C. Wang, J.-G. Liu, X.-D. Zhao, J. Zhong, Y.-X. Li, J. Li, P. Wang, *J. Colloid Interface Sci.* 506 (2017) 437–441.
- [13] J.-J. Li, C.-C. Wang, H.-f. Fu, J.-R. Cui, P. Xu, J. Guo, J.-R. Li, *Dalton Trans.* 46 (2017) 10197–10201.
- [14] D. Sheng, L. Zhu, C. Xu, C. Xiao, Y. Wang, Y. Wang, L. Chen, J. Diwu, J. Chen, Z. Chai, T.E. Albrecht-Schmitt, S. Wang, *Environ. Sci. Technol.* 51 (2017) 3471–3479.
- [15] X. Zhao, Y. Wei, H. Zhao, Z. Gao, Y. Zhang, L. Zhi, Y. Wang, H. Huang, *J. Colloid Interface Sci.* 514 (2018) 234–239.
- [16] Y. Peng, Y. Zhang, H. Huang, C. Zhong, *Chem. Eng. J.* 333 (2018) 678–685.
- [17] L. Liang, L. Liu, F. Jiang, C. Liu, D. Yuan, Q. Chen, D. Wu, H.-L. Jiang, M. Hong, *Inorg. Chem.* 57 (2018) 4891–4897.
- [18] Q. Yang, B. Wang, Y. Chen, Y. Xie, J. Li, *Chin. Chem. Lett.* 30 (2019) 234–238.
- [19] C.C. Wang, Y.S. Ho, *Scientometrics* 109 (2016) 481–513.
- [20] H. Fu, Z. Wang, X. Wang, P. Wang, C.-C. Wang, *CrystEngComm* 20 (2018) 1473–1477.
- [21] X.-D. Du, W. Zheng, X.-H. Yi, J.-P. Zhao, P. Wang, C.-C. Wang, *CrystEngComm* 20 (2018) 2608–2616.
- [22] H. Fu, X. Wang, P. Wang, Z. Wang, H. Ren, C.-C. Wang, *Dalton Trans.* 47 (2018) 9014–9020.
- [23] A. Liu, C.-Z. Wang, C. Chu, H.-Y. Chu, X. Chen, A.-F. Du, J. Mao, W. Zheng, C.-C. Wang, *J. Environ. Chem. Eng.* 6 (2018) 4961–4969.
- [24] X. Yang, J. Qin, Y. Jiang, R. Li, Y. Li, H. Tang, *RSC Adv.* 4 (2014) 18627–18636.
- [25] D. Ma, B. Li, Z. Shi, *Chin. Chem. Lett.* 29 (2018) 827–830.
- [26] X.-Y. Ren, L.-H. Lu, *Chin. Chem. Lett.* 26 (2015) 1439–1445.
- [27] J. Li, Y. Wang, Y. Yu, Q. Li, *Chin. Chem. Lett.* 29 (2018) 837–841.
- [28] C.-C. Wang, X.-D. Du, J. Li, X.-X. Guo, P. Wang, J. Zhang, *Appl. Catal. B: Environ.* 193 (2016) 198–216.
- [29] C.-C. Wang, J.-R. Li, X.-L. Lv, Y.-Q. Zhang, G. Guo, *Energy Environ. Sci.* 7 (2014) 2831–2867.
- [30] H.-P. Jing, C.-C. Wang, Y.-W. Zhang, P. Wang, R. Li, *Rsc Adv.* 4 (2014) 54454–54462.
- [31] C.-C. Wang, Y.-Q. Zhang, J. Li, P. Wang, *J. Mol. Struct.* 1083 (2015) 127–136.
- [32] X.-H. Yi, F.-X. Wang, X.-D. Du, H. Fu, C.-C. Wang, *Polyhedron* 152 (2018) 216–224.
- [33] L. Zhu, D. Sheng, C. Xu, X. Dai, M.A. Silver, J. Li, P. Li, Y. Wang, Y. Wang, L. Chen, C. Xiao, J. Chen, R. Zhou, C. Zhang, O.K. Farha, Z. Chai, T.E. Albrecht-Schmitt, S. Wang, *J. Am. Chem. Soc.* 139 (2017) 14873–14876.
- [34] X. Fang, Q. Shang, Y. Wang, L. Jiao, T. Yao, Y. Li, Q. Zhang, Y. Luo, H.-L. Jiang, *Adv. Mater.* 30 (2018) 1705112.
- [35] C. Xu, K. Sun, Y.-X. Zhou, X. Ma, H.-L. Jiang, *Chem. Commun.* 54 (2018) 2498–2501.
- [36] D. Li, S.-H. Yu, H.-L. Jiang, *Adv. Mater.* 30 (2018) 1707377.
- [37] Z. Han, W. Shi, P. Cheng, *Chin. Chem. Lett.* 29 (2018) 819–822.
- [38] A. Dhakshinamoorthy, Z. Li, H. Garcia, *Chem. Soc. Rev.* 47 (2018) 8134–8172.
- [39] D. Wang, J. Alberio, H. García, Z. Li, *J. Catal.* 349 (2017) 156–162.
- [40] L. Zeng, X. Guo, C. He, C. Duan, *ACS Catal.* 6 (2016) 7935–7947.
- [41] Y. Chen, D. Wang, X. Deng, Z. Li, *Catal. Sci. Technol.* 7 (2017) 4893–4904.
- [42] X. Deng, M. Hao, Z. Li, *Curr. Org. Chem.* 22 (2018) 1825–1835.
- [43] F.X.L.L. Xamena, A. Corma, H. Garcia, *J. Phys. Chem. C* 111 (2007) 80–85.
- [44] Y. Li, H. Xu, S. Ouyang, J. Ye, *Phys. Chem. Chem. Phys.* 18 (2016) 7563–7572.
- [45] J.-L. Wang, C. Wang, W. Lin, *ACS Catal.* 2 (2012) 2630–2640.
- [46] X. Liang, L. Chen, L. Zhang, C.Y. Su, S.O. Chemistry, S.Y.-S. University, *Chin. Sci. Bull.* 63 (2018) 248–265.
- [47] A. Mercedes, C. Esther, F. Belén, F.X. Xamena, I. Llabrés, G. Hermenegildo, *Chemistry* 13 (2010) 5106–5112.
- [48] S. Wang, X. Wang, *Small* 11 (2015) 3097–3112.
- [49] T. Zhang, W. Lin, *Struct. Bond.* 157 (2013) 89–104.
- [50] S. Yuan, J.-S. Qin, H.-Q. Xu, J. Su, D. Rossi, Y. Chen, L. Zhang, C. Lollar, Q. Wang, H.-L. Jiang, D.H. Son, H. Xu, Z. Huang, X. Zou, H.-C. Zhou, *ACS Central Sci.* 4 (2018) 105–111.
- [51] M. Ding, H.-L. Jiang, *ACS Catal.* 8 (2018) 3194–3201.
- [52] D. Sun, Y. Gao, J. Fu, X. Zeng, Z. Chen, Z. Li, *Chem. Commun.* 51 (2015) 2645–2648.
- [53] D. Wang, M. Wang, Z. Li, *ACS Catal.* 5 (2015) 6852–6857.
- [54] D. Wang, Z. Li, *Catal. Sci. Technol.* 5 (2015) 1623–1628.
- [55] D. Wang, Z. Li, *J. Catal.* 342 (2016) 151–157.
- [56] D. Wang, Y. Pan, L. Xu, Z. Li, *J. Catal.* 361 (2018) 248–254.
- [57] J.-D. Xiao, H.-L. Jiang, *Acc. Chem. Res.* (2018), <https://doi.org/10.1021/acs.accounts.1028b00521>.
- [58] D. Wang, Z. Li, *Res. Chem. Intermed.* 43 (2017) 5169–5186.
- [59] Q. Xia, H. Wang, B. Huang, X. Yuan, J. Zhang, J. Zhang, L. Jiang, T. Xiong, G. Zeng, *Small* (2018) 1803088.
- [60] S. Subhadeep, D. Gobinda, T. Jayshri, B. Rahul, *J. Am. Chem. Soc.* 136 (2014) 14845–14851.
- [61] G. Dong, Y. Zhang, Q. Pan, J. Qiu, *J. Photochem. Photobiol. C* 20 (2014) 33–50.
- [62] W. Ho, Z. Zhang, M. Xu, X. Zhang, X. Wang, Y. Huang, *Appl. Catal. B: Environ.* 179 (2015) 106–112.
- [63] F. Dong, L. Wu, Y. Sun, M. Fu, Z. Wu, S.C. Lee, *J. Mater. Chem.* 21 (2011) 15171–15174.
- [64] G. Mamba, A.K. Mishra, *Appl. Catal. B: Environ.* 198 (2016) 347–377.
- [65] Y. Cui, Z. Ding, P. Liu, M. Antonietti, X. Fu, X. Wang, *Phys. Chem. Chem. Phys.* 14 (2012) 1455–1462.
- [66] S. Cao, J. Yu, *J. Phys. Chem. Lett.* 5 (2014) 2101–2107.
- [67] J. Fu, J. Yu, C. Jiang, B. Cheng, *Adv. Energy Mater.* 8 (2018) 1701503.
- [68] W.-J. Ong, L.-L. Tan, Y.H. Ng, S.-T. Yong, S.-P. Chai, *Chem. Rev.* 116 (2016)

- 7159–7329.
- [69] K.S. Lakhi, D.-H. Park, K. Al-Bahily, W. Cha, B. Viswanathan, J.-H. Choy, A. Vinu, *Chem. Soc. Rev.* 46 (2017) 72–101.
 - [70] Y. Chen, Z. Zhan, J. Wang, Y. Shen, S. Liu, Y. Zhang, *Chin. Chem. Lett.* 29 (2018) 437–440.
 - [71] B. Zhu, P. Xia, W. Ho, J. Yu, *Appl. Surf. Sci.* 344 (2015) 188–195.
 - [72] M. Groenewolt, M. Antonietti, *Adv. Mater.* 17 (2005) 1789–1792.
 - [73] H. Montigaud, B. Tanguy, G. Demazeau, I. Alves, S. Courjault, *J. Mater. Sci.* 35 (2000) 2547–2552.
 - [74] J. Wen, J. Xie, X. Chen, X. Li, *Appl. Surf. Sci.* 391 (2017) 72–123.
 - [75] S. Cao, J. Low, J. Yu, M. Jaroniec, *Adv. Mater.* 27 (2015) 2150–2176.
 - [76] D. Masih, Y. Ma, S. Rohani, *Appl. Catal. B: Environ.* 206 (2017) 556–588.
 - [77] S. Zhao, X. Zhao, S. Ouyang, Y. Zhu, *Catal. Sci. Technol.* 8 (2018) 1686–1695.
 - [78] Y. Wang, X. Zhao, Y. Tian, Y. Wang, A.K. Jan, Y. Chen, *Chem. Eur. J.* 23 (2017) 419–426.
 - [79] Y. Wang, J. Sun, J. Li, X. Zhao, *Langmuir* 33 (2017) 4694–4701.
 - [80] J. Zhu, P. Xiao, H. Li, S.A.C. Carabineiro, *ACS Appl. Mater. Interfaces* 6 (2014) 16449–16465.
 - [81] X.-H. Li, J.-S. Chen, X. Wang, J. Sun, M. Antonietti, *J. Am. Chem. Soc.* 133 (2011) 8074–8077.
 - [82] D. Deng, K.S. Novoselov, Q. Fu, N. Zheng, Z. Tian, X. Bao, *Nat. Nanotechnol.* 11 (2016) 218–230.
 - [83] S. Ye, R. Wang, M.-Z. Wu, Y.-P. Yuan, *Appl. Surf. Sci.* 358 (2015) 15–27.
 - [84] L. Ge, C. Han, *Appl. Catal. B: Environ.* 117–118 (2012) 268–274.
 - [85] A. Pisanu, A. Speltini, B. Viganì, F. Ferrari, M. Mannini, N. Calisi, B. Cortigiani, A. Caneschi, P. Quadrelli, A. Profumo, L. Malavasi, *Dalton Trans.* 47 (2018) 6772–6778.
 - [86] C. Zhang, Y. Zhou, J. Bao, J. Fang, S. Zhao, Y. Zhang, X. Sheng, W. Chen, *Chem. Eng. J.* 346 (2018) 226–237.
 - [87] Y. He, Y. Wang, L. Zhang, B. Teng, M. Fan, *Appl. Catal. B: Environ.* 168–169 (2015) 1–8.
 - [88] L. Ye, D. Wu, K.H. Chu, B. Wang, H. Xie, H.Y. Yip, P.K. Wong, *Chem. Eng. J.* 304 (2016) 376–383.
 - [89] D. Xiao, K. Dai, Y. Qu, Y. Yin, H. Chen, *Appl. Surf. Sci.* 358 (2015) 181–187.
 - [90] K. Wei, K. Li, Z. Zeng, Y. Dai, L. Yan, H. Guo, X. Luo, *Chin. J. Catal.* 38 (2017) 1804–1811.
 - [91] X. Wang, Y. Liang, W. An, J. Hu, Y. Zhu, W. Cui, *Appl. Catal. B: Environ.* 219 (2017) 53–62.
 - [92] Q. Sun, X. Hu, S. Zheng, J. Zhang, J. Sheng, *Environ. Pollut.* 245 (2019) 53–62.
 - [93] A. Kumar, A. Kumar, G. Sharma, A.A.H. Al-Muhtaseb, M. Naushad, A.A. Ghfar, C. Guo, F.J. Stadler, *Chem. Eng. J.* 339 (2018) 393–410.
 - [94] Y. Wei, Q. Zou, P. Ye, M. Wang, X. Li, A. Xu, *Chemosphere* 208 (2018) 358–365.
 - [95] S.C. Yan, Z.S. Li, Z.G. Zou, *Langmuir* 25 (2009) 10397–10401.
 - [96] S. Vadeivel, D. Maruthamani, A. Habibi-Yangjeh, B. Paul, S.S. Dhar, K. Selvam, *J. Colloid Interface Sci.* 480 (2016) 126–136.
 - [97] A. Naseri, M. Samadi, A. Pourjavadi, A.Z. Moshfegh, S. Ramakrishna, *J. Mater. Chem. A* 5 (2017) 23406–23433.
 - [98] N. Boonprakob, N. Wetchakun, S. Phanichphant, D. Waxler, P. Sherrell, A. Nattestad, J. Chen, B. Inceesungvorn, *J. Colloid Interface Sci.* 417 (2014) 402–409.
 - [99] L. Gu, J. Wang, Z. Zou, X. Han, J. Hazard. Mater. 268 (2014) 216–223.
 - [100] Y.-F. Shen, C. Zhang, C.-G. Yan, H.-Q. Chen, Y.-J. Zhang, *Chin. Chem. Lett.* 28 (2017) 1312–1317.
 - [101] H.-S. Zhai, L. Cao, X.-H. Xia, *Chin. Chem. Lett.* 24 (2013) 103–106.
 - [102] L. Jiang, X. Yuan, Y. Pan, J. Liang, G. Zeng, Z. Wu, H. Wang, *Appl. Catal. B: Environ.* 217 (2017) 388–406.
 - [103] J. Li, B. Shen, Z. Hong, B. Lin, B. Gao, Y. Chen, *Chem. Commun.* 48 (2012) 12017–12019.
 - [104] L. Shi, K. Chang, H. Zhang, X. Hai, L. Yang, T. Wang, J. Ye, *Small* 12 (2016) 4431–4439.
 - [105] Z. Lin, X. Wang, *Angew. Chem. Int. Ed.* 125 (2013) 1779–1782.
 - [106] W. Chen, T.-Y. Liu, T. Huang, X.-H. Liu, X.-J. Yang, *Nanoscale* 8 (2016) 3711–3719.
 - [107] R. Wang, L. Gu, J. Zhou, X. Liu, F. Teng, C. Li, Y. Shen, Y. Yuan, *Adv. Mater. Interfaces* 2 (2015) 1500037.
 - [108] S. Li, W. Tao, H. Zhang, K. Chang, J. Ye, *Adv. Funct. Mater.* 25 (2015) 5360–5367.
 - [109] S. Liu, F. Chen, S. Li, X. Peng, Y. Xiong, *Appl. Catal. B: Environ.* 211 (2017) 1–10.
 - [110] L. Tian, X. Yang, Q. Liu, F. Qu, H. Tang, *Appl. Surf. Sci.* 455 (2018) 403–409.
 - [111] S. Panneri, M. Thomas, P. Ganguly, B.N. Nair, A.P. Mohamed, K.G.K. Warriar, U.S. Hareesh, *Catal. Sci. Technol.* 7 (2017) 2118–2128.
 - [112] X. Liu, J. Zhang, Y. Dong, H. Li, Y. Xia, H. Wang, *New J. Chem.* 42 (2018) 12180–12187.
 - [113] X. Zhang, Y. Yang, W. Huang, Y. Yang, Y. Wang, C. He, N. Liu, M. Wu, L. Tang, *Mater. Res. Bull.* 99 (2018) 349–358.
 - [114] Y. Zhang, J. Zhou, Q. Feng, X. Chen, Z. Hu, *Chemosphere* 212 (2018) 523–532.
 - [115] D. Guo, R. Wen, M. Liu, H. Guo, J. Chen, W. Weng, *Appl. Organomet. Chem.* 29 (2015) 690–697.
 - [116] C. Bai, J. Bi, J. Wu, H. Meng, Y. Xu, Y. Han, X. Zhang, *Appl. Organomet. Chem.* (2018), <https://doi.org/10.1002/aoc.4597>.
 - [117] J. Huang, X. Zhang, H. Song, C. Chen, F. Han, C. Wen, *Appl. Surf. Sci.* 441 (2018) 85–98.
 - [118] J. Hong, C. Chen, F.E. Bedoya, G.H. Kelsall, D. O'Hare, C. Petit, *Catal. Sci. Technol.* 6 (2016) 5042–5051.
 - [119] X.-D. Du, X.-H. Yi, P. Wang, J. Deng, C.-C. Wang, *Chin. J. Catal.* 40 (2019) 70–79.
 - [120] B. Liu, Y. Wu, X. Han, J. Lv, J. Zhang, H. Shi, *J. Mater. Sci.: Mater. Electron.* 29 (2018) 17591–17601.
 - [121] Y. Gong, B. Yang, H. Zhang, X. Zhao, *J. Mater. Chem. A* 6 (2018) 23703–23711.
 - [122] H. Wang, X. Yuan, Y. Wu, G. Zeng, X. Chen, L. Leng, H. Li, *Appl. Catal. B: Environ.* 174–175 (2015) 445–454.
 - [123] D.A. Giannakoudakis, N.A. Travlou, J. Secor, T.J. Bandoz, *Small* 13 (2017) 201601758.
 - [124] X. Li, Y. Pi, L. Wu, Q. Xia, J. Wu, Z. Li, J. Xiao, *Appl. Catal. B: Environ.* 202 (2017) 653–663.
 - [125] Z.-D. Lei, Y.-C. Xue, W.-Q. Chen, L. Li, W.-H. Qiu, Y. Zhang, L. Tang, *Small* 14 (2018) 1802045.
 - [126] X.-H. Yi, F.-X. Wang, X.-D. Du, P. Wang, C.-C. Wang, *Appl. Organomet. Chem.* 32 (2018) e4621.
 - [127] K.S. Park, Z. Ni, A.P. Côté, J.Y. Choi, R. Huang, F.J. Uribe-Romo, H.K. Chae, M. O'Keeffe, O.M. Yaghi, *Proc. Natl. Acad. Sci.* 103 (2006) 10186–10191.
 - [128] S. Gadipelli, W. Travis, W. Zhou, Z. Guo, *Energy Environ. Sci.* 7 (2014) 2232–2238.
 - [129] C. Chen, J. Kim, D.A. Yang, W.S. Ahn, *Chem. Eng. J.* 168 (2011) 1134–1139.
 - [130] G. Kumari, K. Jayaramulu, T.K. Maji, C. Narayana, *J. Phys. Chem. A* 117 (2013) 11006–11012.
 - [131] Q. Song, S.K. Nataraj, M.V. Roussanova, J.C. Tan, D.J. Hughes, W. Li, P. Bourgoign, M.A. Alam, A.K. Cheetham, S.A. Almuhtaseb, *Energy Environ. Sci.* 5 (2012) 8359–8369.
 - [132] C. Hu, W. Xu, X. Mo, H. Li, S. Zhou, P. Zhang, K. Tang, *Adsorption* 24 (2018) 733–744.
 - [133] U.P.N. Tran, K.K.A. Le, N.T.S. Phan, *ACS Catal.* 1 (2011) 120–127.
 - [134] P.Z. Li, K. Aranishi, Q. Xu, *Chem. Commun.* 48 (2012) 3173–3175.
 - [135] S. Liu, Z. Xiang, Z. Hu, X. Zheng, D. Cao, *J. Mater. Chem.* 21 (2011) 6649–6653.
 - [136] Y. Zhang, S.-J. Park, *Appl. Catal. B: Environ.* 240 (2019) 92–101.
 - [137] M. Zhang, Q. Shang, Y. Wan, Q. Cheng, G. Liao, Z. Pan, *Appl. Catal. B: Environ.* 241 (2019) 149–158.
 - [138] G. Fan, X. Zheng, J. Luo, H. Peng, H. Lin, M. Bao, L. Hong, J. Zhou, *Chem. Eng. J.* 351 (2018) 782–790.
 - [139] G. Fan, J. Luo, L. Guo, R. Lin, X. Zheng, S.A. Snyder, *Chemosphere* 209 (2018) 44–52.
 - [140] J. Qiu, X.-F. Zhang, X. Zhang, Y. Feng, Y. Li, L. Yang, H. Lu, J. Yao, J. Hazard. Mater. 349 (2018) 234–241.
 - [141] X. Yang, Z. Wen, Z. Wu, X. Luo, *Inorg. Chem. Front.* 5 (2018) 687–693.
 - [142] J. Gao, Y. Zhou, Z. Li, S. Yan, N. Wang, Z. Zou, *Nanoscale* 4 (2012) 3687–3692.
 - [143] J. Cravillon, R. Nayuk, S. Springer, A. Feldhoff, K. Huber, M. Wiebecke, *Chem. Mater.* 23 (2011) 2130–2141.
 - [144] X. Wang, K. Maeda, A. Thomas, K. Takanabe, G. Xin, J.M. Carlsson, K. Domen, M. Antonietti, *Nat. Mater.* 8 (2009) 76–80.
 - [145] P. Xia, B. Zhu, J. Yu, S. Cao, M. Jaroniec, *J. Mater. Chem. A* 5 (2017) 3230–3238.
 - [146] Y. Zheng, L. Lin, B. Wang, X. Wang, *Angew. Chem. Int. Ed.* 54 (2015) 12868–12884.
 - [147] M. Marszewski, S. Cao, J. Yu, M. Jaroniec, *Mater. Horiz.* 2 (2015) 261–278.
 - [148] X. Li, J. Wen, J. Low, Y. Fang, J. Yu, *Sci. China Mater.* 57 (2014) 70–100.
 - [149] X. Wang, J. Liu, S. Leong, X. Lin, J. Wei, B. Kong, Y. Xu, Z.-X. Low, J. Yao, H. Wang, *ACS Appl. Mater. Interfaces* 8 (2016) 9080–9087.
 - [150] X. Zeng, L. Huang, C. Wang, J. Wang, J. Li, X. Luo, *ACS Appl. Mater. Interfaces* 8 (2016) 20274–20282.
 - [151] M.E. Parolo, M.C. Savini, J.M. Vallés, M.T. Baschini, M.J. Avena, *Appl. Clay Sci.* 40 (2008) 179–186.
 - [152] J.H. Cavka, S. Jakobsen, U. Olsbye, N. Guillou, C. Lamberti, S. Bordiga, K.P. Lillerud, *J. Am. Chem. Soc.* 130 (2008) 13850–13851.
 - [153] H. Wu, T. Yildirim, W. Zhou, *J. Phys. Chem. Lett.* 4 (2013) 925–930.
 - [154] A.D. Wiersum, E. Soubeyrand-Lenoir, Q. Yang, B. Moulin, V. Guillermin, M.B. Yahia, S. Bourrelly, A. Vimont, S. Miller, C. Vagner, M. Daturi, G. Clet, C. Serre, G. Maurin, P.L. Llewellyn, *Chem. Asian J.* 6 (2011) 3270–3280.
 - [155] L. Valenzano, B. Civalieri, S. Chavan, S. Bordiga, M.H. Nilsen, S. Jakobsen, K.P. Lillerud, C. Lamberti, *Chem. Mater.* 23 (2011) 1700–1718.
 - [156] W. Fu-Xue, W. Chong-Chen, W. Peng, X. Bi-Cong, *Chin. J. Inorg. Chem.* 33 (2017) 713–737.
 - [157] S.-N. Kim, Y.-R. Lee, S.-H. Hong, M.-S. Jang, W.-S. Ahn, *Catal. Today* 245 (2015) 54–60.
 - [158] F. Vermoortele, B. Bueken, G.L. Le Bars, B. Van de Voorde, M. Vandichel, K. Houthoofd, A. Vimont, M. Daturi, M. Waroquier, V. Van Speybroeck, *J. Am. Chem. Soc.* 135 (2013) 11465–11468.
 - [159] D. Sun, Y. Fu, W. Liu, L. Ye, D. Wang, L. Yang, X. Fu, Z. Li, *Chem. Eur. J.* 19 (2013) 14279–14285.
 - [160] L. Shen, W. Wu, R. Liang, R. Lin, L. Wu, *Nanoscale* 5 (2013) 9374–9382.
 - [161] C.G. Silva, I. Luz, F.X. Llabrés i Xamena, A. Corma, H. García, *Chem.-Eur. J.* 16 (2010) 11133–11138.
 - [162] J. Long, S. Wang, Z. Ding, S. Wang, Y. Zhou, L. Huang, X. Wang, *Chem. Commun.* 48 (2012) 11656–11658.
 - [163] L. Shen, S. Liang, W. Wu, R. Liang, L. Wu, *J. Mater. Chem. A* 1 (2013) 11473–11482.
 - [164] D. Sun, Z. Li, *Chin. J. Chem.* 35 (2017) 135–147.
 - [165] S. Chavan, J.G. Vitillo, D. Gianolio, O. Zavorotynska, B. Civalieri, S. Jakobsen, M.H. Nilsen, L. Valenzano, C. Lamberti, K.P. Lillerud, S. Bordiga, *Phys. Chem. Chem. Phys.* 14 (2012) 1614–1626.
 - [166] H.R. Abid, H. Tian, H.-M. Ang, M.O. Tade, C.E. Buckley, S. Wang, *Chem. Eng. J.* 187 (2012) 415–420.
 - [167] Q. Yang, V. Guillermin, F. Ragon, A.D. Wiersum, P.L. Llewellyn, C. Zhong, T. Devic, C. Serre, G. Maurin, *Chem. Commun.* 48 (2012) 9831–9833.
 - [168] N. Chang, X.-P. Yan, *J. Chromatogr. A* 1257 (2012) 116–124.
 - [169] Y.-Y. Fu, C.-X. Yang, X.-P. Yan, *Chem. Commun.* 49 (2013) 7162–7164.

- [170] Y.S. Seo, N.A. Khan, S.H. Jhung, *Chem. Eng. J.* 270 (2015) 22–27.
- [171] Y. Horiuchi, T. Toyao, M. Saito, K. Mochizuki, M. Iwata, H. Higashimura, M. Anpo, M. Matsuoka, *J. Phys. Chem. C* 116 (2012) 20848–20853.
- [172] M.A. Nasalevich, C.H. Hendon, J.G. Santaclara, K. Svane, B. van der Linden, S.L. Weber, M.V. Fedin, A.J. Houtepen, M.A. van der Veen, F. Kapteijn, A. Walsh, *J. Gascon, Sci. Rep.* 6 (2016) 23676.
- [173] A. Santiago Portillo, H.G. Baldoví, M.T. García Fernandez, S. Navalón, P. Atienzar, B. Ferrer, M. Alvaro, H. Garcia, Z. Li, *J. Phys. Chem. C* 121 (2017) 7015–7024.
- [174] X. Xu, R. Liu, Y. Cui, X. Liang, C. Lei, S. Meng, Y. Ma, Z. Lei, Z. Yang, *Appl. Catal. B Environ.* 210 (2017) 484–494.
- [175] F. Millange, C. Serre, G. Férey, *Chem. Commun.* 8 (2002) 822–823.
- [176] G. Férey, M. Latroche, C. Serre, F. Millange, T. Loiseau, A. Percheron-Guégan, *Chem. Commun.* 24 (2003) 2976–2977.
- [177] L. Hamon, C. Serre, T. Devic, T. Loiseau, F. Millange, G. Férey, G.D. Weireld, *J. Am. Chem. Soc.* 131 (2009) 8775–8777.
- [178] P.L. Llewellyn, P. Horcajada, G. Maurin, T. Devic, N. Rosenbach, S. Bourrelly, C. Serre, D. Vincent, S. Loera-Serna, Y. Filinchuk, G. Férey, *J. Am. Chem. Soc.* 131 (2009) 13002–13008.
- [179] G. de Combarieu, M. Morcrette, F. Millange, N. Guillo, J. Cabana, C.P. Grey, I. Margiolaki, G. Férey, J.M. Tarascon, *Chem. Mater.* 21 (2009) 1602–1611.
- [180] F. Millange, N. Guillo, M.E. Medina, G. Férey, A. Carlin-Sinclair, K.M. Golden, R.I. Walton, *Chem. Mater.* 22 (2010) 4237–4245.
- [181] X.-F. Chen, H. Zhang, X. Wang, J.-G. Cheng, R.-S. Zhao, C.-G. Cheng, X.-Q. Lu, *Analyst* 137 (2012) 5411–5419.
- [182] S. Bourrelly, B. Moulin, A. Rivera, G. Maurin, S. Devautour-Vinot, C. Serre, T. Devic, P. Horcajada, A. Vimont, G. Clet, J.-C. Lavalley, S. Loera-Serna, R. Denoyel, P.L. Llewellyn, G. Férey, *J. Am. Chem. Soc.* 132 (2010) 9488–9498.
- [183] T.K. Trung, P. Trens, N. Tanchoux, S. Bourrelly, P.L. Llewellyn, S. Loera-Serna, C. Serre, T. Loiseau, F. Fajula, G. Férey, *J. Am. Chem. Soc.* 130 (2008) 16926–16932.
- [184] D.V. Patil, P.B.S. Rallapalli, G.P. Dangi, R.J. Tayade, R.S. Somani, H.C. Bajaj, *Ind. Eng. Chem. Res.* 50 (2011) 10516–10524.
- [185] L. Ai, L. Li, C. Zhang, J. Fu, J. Jiang, *Chem. Eur. J.* 19 (2013) 15105–15108.
- [186] S. Couck, J.F. Denayer, G.V. Baron, T. Rémy, J. Gascon, F. Kapteijn, *J. Am. Chem. Soc.* 131 (2009) 6326–6327.
- [187] V. Finsy, L. Ma, L. Alaerts, D. De Vos, G. Baron, J. Denayer, *Microporous Mesoporous Mater.* 120 (2009) 221–227.
- [188] J. Jia, F. Xu, Z. Long, X. Hou, M.J. Sepaniak, *Chem. Commun.* 49 (2013) 4670–4672.
- [189] J.-J. Du, Y.-P. Yuan, J.-X. Sun, F.-M. Peng, X. Jiang, L.-G. Qiu, A.-J. Xie, Y.-H. Shen, J.-F. Zhu, *J. Hazard. Mater.* 190 (2011) 945–951.
- [190] L. Ai, C. Zhang, L. Li, J. Jiang, *Appl. Catal. B: Environ.* 148–149 (2014) 191–200.
- [191] R. Liang, F. Jing, L. Shen, N. Qin, L. Wu, *J. Hazard. Mater.* 287 (2015) 364–372.
- [192] X. Feng, H. Chen, F. Jiang, *J. Colloid Interface Sci.* 494 (2017) 32–37.
- [193] Z. Jia, M. Jiang, G. Wu, *Chem. Eng. J.* 307 (2017) 283–290.
- [194] K.G.M. Laurier, F. Vermoortele, R. Ameloot, D.E. De Vos, J. Hofkens, M.B.J. Roeffaers, *J. Am. Chem. Soc.* 135 (2013) 14488–14491.
- [195] D. Wang, R. Huang, W. Liu, D. Sun, Z. Li, *ACS Catal.* 4 (2014) 4254–4260.
- [196] L. Chi, Q. Xu, X. Liang, J. Wang, X. Su, *Small* 12 (2016) 1351–1358.
- [197] H. Lv, H. Zhao, T. Cao, L. Qian, Y. Wang, G. Zhao, *J. Mol. Catal. A: Chem.* 400 (2015) 81–89.
- [198] M. Cheng, C. Lai, Y. Liu, G. Zeng, D. Huang, C. Zhang, L. Qin, L. Hu, C. Zhou, W. Xiong, *Coord. Chem. Rev.* 368 (2018) 80–92.
- [199] C. Petit, T.J. Bandoz, *Adv. Funct. Mater.* 21 (2011) 2108–2117.
- [200] C.-F. Zhang, L.-G. Qiu, F. Ke, Y.-J. Zhu, Y.-P. Yuan, G.-S. Xu, X. Jiang, *J. Mater. Chem. A* 1 (2013) 14329–14334.
- [201] R. Liang, F. Jing, L. Shen, N. Qin, L. Wu, *Nano Res.* 8 (2015) 3237–3249.
- [202] P. Niu, L. Zhang, G. Liu, H.M. Cheng, *Adv. Funct. Mater.* 22 (2012) 4763–4770.
- [203] X. Zhang, X. Xie, H. Wang, J. Zhang, B. Pan, Y. Xie, *J. Am. Chem. Soc.* 135 (2013) 18–21.
- [204] F. Ke, L. Wang, J. Zhu, *Nano Res.* 8 (2015) 1834–1846.
- [205] N. Daneshvar, D. Salari, A.R. Khataee, *J. Photochem. Photobiol., A* 162 (2004) 317–322.
- [206] P. Pichat, C. Guillard, L. Amalric, A.C. Renard, O. Plaidy, *Sol. Energy Mater. Sol. Cells* 38 (1995) 391–399.
- [207] J. Huang, H. Song, C. Chen, Y. Yang, N. Xu, X. Ji, C. Li, J.-A. You, *J. Environ. Chem. Eng.* 5 (2017) 2579–2585.
- [208] F. Ning, M. Shao, S. Xu, Y. Fu, R. Zhang, M. Wei, D.G. Evans, X. Duan, *Energy Environ. Sci.* 9 (2016) 2633–2643.
- [209] Z. Wang, Z. Jin, H. Yuan, G. Wang, B. Ma, *J. Colloid Interface Sci.* 532 (2018) 287–299.
- [210] Q. Liang, S. Cui, J. Jin, C. Liu, S. Xu, C. Yao, Z. Li, *Appl. Surf. Sci.* 456 (2018) 899–907.
- [211] Q. Liang, J. Jin, C. Liu, S. Xu, C. Yao, Z. Li, *Inorg. Chem. Front.* 5 (2018) 335–343.
- [212] X. Zhang, H. Dong, X.-J. Sun, D.-D. Yang, J.-L. Sheng, H.-L. Tang, X.-B. Meng, F.-M. Zhang, *ACS Sustain. Chem. Eng.* 6 (2018) 11563–11569.
- [213] F. Wang, Y.T. Zhang, Y. Xu, X. Wang, S. Li, H. Yang, X. Liu, F. Wei, *J. Environ. Chem. Eng.* 4 (2016) 3364–3373.
- [214] H.-L. Jiang, Y. Pan, D. Li, *Chem. Eur. J.* 24 (2018) 18403.
- [215] Z. Wang, Z. Jin, G. Wang, B. Ma, *Int. J. Hydrogen Energy* 43 (2018) 13039–13050.
- [216] J. Xu, J. Gao, C. Wang, Y. Yang, L. Wang, *Appl. Catal. B: Environ.* 219 (2017) 101–108.
- [217] Z. Yang, X. Xu, X. Liang, C. Lei, Y. Cui, W. Wu, Y. Yang, Z. Zhang, Z. Lei, *Appl. Catal. B: Environ.* 205 (2017) 42–54.
- [218] Y. Zhang, Z. Jin, A. Iuan, G. Wang, *Int. J. Hydrogen Energy* 43 (2018) 9914–9923.
- [219] S. Liu, L. Ma, H. Zhang, C. Ma, *Mater. Res. Bull.* 77 (2016) 271–278.
- [220] W.-Z. Gao, Y. Xu, Y. Chen, W.-F. Fu, *Chem. Commun.* 51 (2015) 13217–13220.
- [221] L. Xiao, T. Su, Z. Wang, K. Zhang, X. Peng, Y. Han, Q. Li, X. Wang, *Nano. Res. Lett.* 13 (2018) 31.
- [222] Z. Jin, H. Yang, *Nano. Res. Lett.* 12 (2017) 539.
- [223] X. Hao, Y. Wang, J. Zhou, Z. Cui, Y. Wang, Z. Zou, *Appl. Catal. B: Environ.* 221 (2018) 302–311.
- [224] L. Ye, X. Liu, Q. Zhao, H. Xie, L. Zan, *J. Mater. Chem. A* 1 (2013) 8978–8983.
- [225] J. Wu, X. Chen, C. Li, Y. Qi, X. Qi, J. Ren, B. Yuan, B. Ni, R. Zhou, J. Zhang, T. Huang, *Chem. Eng. J.* 304 (2016) 533–543.
- [226] D. Kandi, S. Martha, A. Thirumurugan, K.M. Parida, *J. Phys. Chem. C* 121 (2017) 4834–4849.
- [227] L. Sun, L. Xiang, X. Zhao, C.-J. Jia, J. Yang, Z. Jin, X. Cheng, W. Fan, *ACS Catal.* 5 (2015) 3540–3551.
- [228] J. Jiang, X. Zhang, P. Sun, L. Zhang, *J. Phys. Chem. C* 115 (2011) 20555–20564.
- [229] X. Zhou, C. Shao, S. Yang, X. Li, X. Guo, X. Wang, X. Li, Y. Liu, *ACS Sustain. Chem. Eng.* 6 (2018) 2316–2323.
- [230] D. Jiang, L. Chen, J. Zhu, M. Chen, W. Shi, J. Xie, *Dalton Trans.* 42 (2013) 15726–15734.
- [231] K. Dai, L. Lu, C. Liang, G. Zhu, Q. Liu, L. Geng, J. He, *Dalton Trans.* 44 (2015) 7903–7910.
- [232] M. Jahurul Islam, H.K. Kim, D. Amarathana Reddy, Y. Kim, R. Ma, H. Baek, J. Kim, T.K. Kim, *Dalton Trans.* 46 (2017) 6013–6023.
- [233] C. Liu, Y. Qiu, F. Wang, K. Wang, Q. Liang, Z. Chen, *Adv. Mater. Interfaces* 4 (2017) 1700681.
- [234] M.F. Kuehn, K.L. Orchard, K.E. Dalle, E. Reisner, *J. Am. Chem. Soc.* 139 (2017) 7217–7223.
- [235] Y. Hao, S.-Z. Kang, X. Liu, X. Li, L. Qin, J. Mu, *ACS Sustain. Chem. Eng.* 5 (2017) 1165–1172.
- [236] K. Li, R. Chen, S.-L. Li, S.-L. Xie, X.-L. Cao, L.-Z. Dong, J.-C. Bao, Y.-Q. Lan, *ACS Appl. Mater. Interfaces* 8 (2016) 4516–4522.
- [237] L. Yao, D. Wei, Y. Ni, D. Yan, C. Hu, *Nano Energy* 26 (2016) 248–256.
- [238] X.-F. Zhang, Y. Chen, Y. Feng, X. Zhang, J. Qiu, M. Jia, J. Yao, *J. Alloys Compd.* 705 (2017) 392–398.
- [239] W. Xue, X. Hu, E. Liu, J. Fan, *Appl. Surf. Sci.* 447 (2018) 783–794.
- [240] Y. Su, Z. Zhang, H. Liu, Y. Wang, *Appl. Catal. B: Environ.* 200 (2017) 448–457.
- [241] H. Liu, Z. Jin, Z. Xu, *Dalton Trans.* 44 (2015) 14368–14375.
- [242] Y.-P. Yuan, L.-S. Yin, S.-W. Cao, G.-S. Xu, C.-H. Li, C. Xue, *Appl. Catal. B: Environ.* 168–169 (2015) 572–576.
- [243] M. Retuerto, A.G. Pereira, F.J. Pérez-Alonso, M.A. Peña, J.L.G. Fierro, J.A. Alonso, M.T. Fernández-Díaz, L. Pascual, S. Rojas, *Appl. Catal. B: Environ.* 203 (2017) 363–371.
- [244] H. Ming, Z. Ma, Y. Liu, K. Pan, H. Yu, F. Wang, Z. Kang, *Dalton Trans.* 41 (2012) 9526–9531.
- [245] P. Yang, J. Zhao, J. Wang, H. Cui, L. Li, Z. Zhu, *RSC Adv.* 5 (2015) 21332–21335.
- [246] Y. Pengju, Z. Jianghong, Z. Lexi, L. Li, Z. Zhenping, *Chemistry* 21 (2015) 8561–8568.
- [247] J. Liu, Y. Liu, N. Liu, Y. Han, X. Zhang, H. Huang, Y. Lifshitz, S.T. Lee, J. Zhong, Z. Kang, *Science* 347 (2015) 970–974.
- [248] G. Gao, Y. Jiao, F. Ma, Y. Jiao, E. Wacławik, A. Du, *Phys. Chem. Chem. Phys.* 17 (2015) 31140–31144.
- [249] Q. Liu, T. Chen, Y. Guo, Z. Zhang, X. Fang, *Appl. Catal. B: Environ.* 193 (2016) 248–258.
- [250] K. Li, F.Y. Su, W.D. Zhang, *Appl. Surf. Sci.* 375 (2016) 110–117.
- [251] S. Fang, X. Yang, K. Lv, L. Qin, S. Jie, L. Mei, *Appl. Catal. B: Environ.* 185 (2016) 225–232.
- [252] W.-J. Ong, L.K. Putri, Y.-C. Tan, L.-L. Tan, N. Li, Y.H. Ng, X. Wen, S.-P. Chai, *Nano Res.* 10 (2017) 1673–1696.
- [253] F. Wang, C. Ping, Y. Feng, Z. Xie, L. Yang, Y. Su, Q. Zhang, Y. Wang, K. Yao, W. Lv, *Appl. Catal. B: Environ.* 207 (2017) 103–113.
- [254] Q. Liu, T. Chen, Y. Guo, Z. Zhang, X. Fang, *Appl. Catal. B: Environ.* 205 (2017) 173–181.
- [255] T. Xiong, W. Cen, Y. Zhang, F. Dong, *ACS Catal.* 6 (2016) 2462–2472.
- [256] P. Niu, L. Zhang, G. Liu, H.M. Cheng, *Adv. Funct. Mater.* 22 (2012) 4763–4770.
- [257] Y. Chen, B. Lin, H. Wang, Y. Yang, H. Zhu, W. Yu, J.-m. Basset, *Chem. Eng. J.* 286 (2016) 339–346.
- [258] A. Thomas, A. Fischer, F. Goettmann, M. Antonietti, J.-O. Müller, R. Schlögl, J.M. Carlsson, *J. Mater. Chem.* 18 (2008) 4893–4908.
- [259] Y. Ma, X. Wang, Y. Jia, X. Chen, H. Han, C. Li, *Chem. Rev.* 114 (2014) 9987–10043.
- [260] L. Ruan, G. Xu, L. Gu, C. Li, Y. Zhu, Y. Lu, *Mater. Res. Bull.* 66 (2015) 156–162.
- [261] W. Zhang, Z. Zhang, F. Zhang, W. Yang, *Appl. Surf. Sci.* 386 (2016) 247–254.
- [262] J. Liu, *J. Phys. Chem. C* 119 (2015) 28417–28423.
- [263] B. Zhu, Z. Zhang, C. Jiang, B. Cheng, J. Yu, *Appl. Catal. B: Environ.* 207 (2017) 27–34.
- [264] S.C. Yan, Z.S. Li, Z.G. Zou, *Langmuir* 26 (2010) 3894–3901.
- [265] G. Liu, P. Niu, C. Sun, S.C. Smith, Z. Chen, G.Q. Lu, H.-M. Cheng, *J. Am. Chem. Soc.* 132 (2010) 11642–11648.
- [266] K. Wang, Q. Li, B. Liu, B. Cheng, W. Ho, J. Yu, *Appl. Catal. B: Environ.* 176–177 (2015) 44–52.
- [267] X. Ma, Y. Lv, J. Xu, Y. Liu, R. Zhang, Y. Zhu, *J. Phys. Chem. C* 116 (2012) 23485–23493.
- [268] H. Yu, L. Shang, T. Bian, R. Shi, G.I.N. Waterhouse, Y. Zhao, C. Zhou, L.-Z. Wu, C.-H. Tung, T. Zhang, *Adv. Mater.* 28 (2016) 5080–5086.
- [269] Y. Deng, L. Tang, G. Zeng, Z. Zhu, M. Yan, Y. Zhou, J. Wang, Y. Liu, *J. Wang, Appl. Catal. B: Environ.* 203 (2017) 343–354.

- [270] J. Xu, K.-Z. Long, Y. Wang, B. Xue, Y.-X. Li, *Appl. Catal. A: Gen.* 496 (2015) 1–8.
- [271] Y. Zheng, L. Lin, X. Ye, F. Guo, X. Wang, *Angew. Chem. Int. Ed.* 53 (2014) 11926–11930.
- [272] S. Feng, P. Yan, L. Xu, J. Xia, H. Li, *Chin. Chem. Lett.* 29 (2018) 1629–1632.
- [273] Q. Huang, J. Yu, S. Cao, C. Cui, B. Cheng, *Appl. Surf. Sci.* 358 (2015) 350–355.
- [274] F.-t. Li, Y. Zhao, Q. Wang, X.-j. Wang, Y.-j. Hao, R.-h. Liu, D. Zhao, *J. Hazard. Mater.* 283 (2015) 371–381.
- [275] W.-J. Ong, L.-L. Tan, S.-P. Chai, S.-T. Yong, A.R. Mohamed, *Nano Energy* 13 (2015) 757–770.
- [276] Y. Kang, Y. Yang, L.-C. Yin, X. Kang, G. Liu, H.-M. Cheng, *Adv. Mater.* 27 (2015) 4572–4577.
- [277] J. Zhang, F. Guo, X. Wang, *Adv. Funct. Mater.* 23 (2013) 3008–3014.
- [278] D. Chen, J. Yang, H. Ding, *Appl. Surf. Sci.* 391 (2017) 384–391.
- [279] Q. Gao, S. Hu, Y. Du, Z. Hu, *J. Mater. Chem. A* 5 (2017) 4827–4834.
- [280] J. Fu, B. Zhu, C. Jiang, B. Cheng, W. You, J. Yu, *Small* 13 (2017) 1603938.
- [281] J. Sun, J. Zhang, M. Zhang, M. Antonietti, X. Fu, X. Wang, *Nat. Commun.* 3 (2012) 1139.
- [282] D. Zheng, C. Huang, X. Wang, *Nanoscale* 7 (2015) 465–470.
- [283] Q. Fan, J. Liu, Y. Yu, S. Zuo, B. Li, *Appl. Surf. Sci.* 391 (2017) 360–368.
- [284] X.-H. Li, J. Zhang, X. Chen, A. Fischer, A. Thomas, M. Antonietti, X. Wang, *Chem. Mater.* 23 (2011) 4344–4348.
- [285] Y. Wang, L. Li, L. Yan, L. Cao, P. Dai, X. Gu, X. Zhao, *Chin. Chem. Lett.* 29 (2018) 849–853.
- [286] C. Vaitsis, G. Sourkouni, C. Argiris, *Ultrason. Sonochem.* (2018), <https://doi.org/10.1016/j.ultsonch.2018.11.004>.
- [287] G. Lan, K. Ni, W. Lin, *Coord. Chem. Rev.* 379 (2019) 65–81.
- [288] H. Li, S. Yao, H.-L. Wu, J.-Y. Qu, Z.-M. Zhang, T.-B. Lu, W. Lin, E.-B. Wang, *Appl. Catal. B: Environ.* 224 (2018) 46–52.
- [289] B. Han, X. Ou, Z. Deng, Y. Song, C. Tian, H. Deng, Y.-J. Xu, Z. Lin, *Angew. Chem. Int. Ed.* 57 (2018) 16811.
- [290] L. Zhang, J. Wang, X. Ren, W. Zhang, T. Zhang, X. Liu, T. Du, T. Li, J. Wang, *J. Mater. Chem. A* 6 (2018) 21029–21038.
- [291] P. Arul, S.A. John, *J. Electroanal. Chem.* 829 (2018) 168–176.
- [292] M. Nasalevich, M. Van der Veen, F. Kapteijn, J. Gascon, *CrystEngComm* 16 (2014) 4919–4926.
- [293] H.A. Lopez, A. Dhakshinamoorthy, B. Ferrer, P. Atienzar, M. Alvaro, H. Garcia, *J. Phys. Chem. C* 115 (2011) 22200–22206.